2022-08-09

Design and Characterization of a Miniaturized Spectrometer for Wearable Applications

Tyler Richard Westover
Brigham Young University

Design and Characterization of a Miniaturized Spectrometer for Wearable Applications

Tyler Richard Westover

A dissertation submitted to the faculty of
Brigham Young University
in partial fulfillment of the requirements for the degree of

Doctor of Philosophy

Robert C. Davis, Chair
Richard R. Vanfleet
Brian Jensen
Tyler Jarvis
Richard Sandberg

Department of Physics and Astronomy

Brigham Young University

ABSTRACT

Design and Characterization of a Miniaturized Spectrometer for Wearable Applications

Tyler Richard Westover
Department of Physics and Astronomy, BYU
Doctor of Philosophy

As individual health monitors continue to become more widely adopted in helping individuals make informed decisions, new technologies need to be developed to obtain more biometric data. Spectroscopy is a well-known tool to gain biological information. Traditionally spectrometers are large and expensive making personal or wearable health monitors difficult. Here we present the development and characterization of a miniaturized short wavelength infrared spectrometer for wearable applications. We present a carbon nanotube parallel hole collimator can effectively select a narrow set of allowed angles of light to be separated by a linear variable filter and detected at a photodiode array making a spectrometer. We will go over the calibration of the spectrometer showing a resolution of 13 nm at 1300 nm. Improvements on the original collimator data will be discussed, including carbon nanotube growth without infiltration and growth on transparent substrates. We will also show measurements made on human subjects yielding a pulse.

Keywords: spectroscopy, carbon nanotubes, parallel hole collimator, CNT-M, wearable

Acknowledgements

I would like to first thank my wife and children for their understanding, love and support as I have worked through this degree. For the time they spent at home during class breaks, so I could continue to work in the lab. Their patience with the long days that sometimes turned into long nights at the lab while collecting data. I would also like to thank the rest of my family for their support and encouragement throughout this whole process, and their attempts to understand my explanations of what I was doing for my research.

I would also like to thank the students that I worked with and the other students in the lab that allowed for conversations about the research into the development of methods to overcome hurdles. Especially the other grad students for their help in the writing process with editing and encouragement.

I would like to thank Tula Health for their funding of this research and the opportunity to work on this interesting project. I would like to thank the department of Physics and Astronomy for the use of facilities and funding of undergraduates who help support this work. I would like to thank the BYU microscopy and cleanroom facilities for their use of equipment and technical support.

Table of Contents

List of Figures

List of Tables

Chapter 1: Introduction

1.1 Health Monitoring

For the last several years health and fitness monitoring has become common in our society. Due to the advancements in miniaturized sensors and electronics, these measurements have grown to encompass a wide variety of physiological signals i.e., SpO2, heartrate, blood pressure and ECG. For individuals with certain pre-existing conditions, health monitoring can be vital to maintaining their standard of health[1]. For example, those with diabetes must regularly monitor their glucose levels through a variety of old and new technologies[2, 3]. These are typically invasive or minimally invasive procedures like finger sticks or continuous glucose monitors[4, 5]. For many even minimally invasive procedures are a deterrent to regular monitoring[6].

Non-invasive physiological monitoring of the body is commonly done via optical measurements[7]. Sensors found on these devices are usually LED-photodiode combinations for measuring heart rate and inertial sensors for determining activity. For these wearable fitness and health monitors to output new types of information, additional types of physiological sensing need to be developed which can be enabled with more versatile and robust miniature sensors[8, 9].

One region of the optical spectrum with untapped potential for measuring physiological information is the short wavelength infrared (SWIR) (900-1700 nm). While near infrared wavelengths are commonly used in applications such as pulse oximetry, the short wavelength infrared has recently received increased attention due to the richness of information available[10, 11]. In this region there are key absorption peaks for biological molecules including glucose, urea,

triacetin and water[10, 12, 13]. As many biological constituents are made up of a limited number of elements (and types of molecular bonds), their interactions with light behave similarly[14], causing a high degree of overlap in absorption features. Miniaturized SWIR spectrometers are able to collect detailed spectra, that could be valuable in identifying the individual molecular concentrations.

1.2 Spectroscopy

Spectroscopy is an invaluable tool for studying materials and the chemical makeup of matter[15]. Recently much work has been done, to both miniaturize and reduce the cost of spectrometers while increasing their availability and use[16, 17]. Spectrometer types can be divided into a few different categories based on the operating principle used to disperse light (either temporally or spatially) and measure wavelength bands. Categories of spectrometers include diffraction grating spectrometers[18], wedge filter spectrometers[19], Fourier transform spectrometers[20], and tunable filter spectrometers[21]. The common requirement is they all need light that is collimated.

1.3 Miniaturization

A primary contributor to the size of traditional spectrometers are the optics that both collimate and separate the light by wavelength. Many spectrometers use angles and optical pathlength as a means to collimate and separate the light by wavelength. Long pathlengths allow for ultra-high-resolution spectrometers. There are many emerging applications for spectrometers that do not require high resolution but would benefit from handheld or portable uses[22, 23]. These applications include dirt and food quality analysis. Further miniaturization would allow new applications in biomedical wearables[17, 24].

1.4 Linear variable filters

Wedge filter-based spectrometers have been studied as one route to miniaturization[19, 25, 26]. Wedge filters typically use Fabry-Perot filters to separate the light by wavelength. Fabry-Perot filters operate by having two parallel mirrors a predetermined distance apart. These mirrors create a resonating cavity from which only select wavelengths can pass through. The selected wavelengths are dictated by the spacing of the mirrors. Multiple Fabry-Perot filters could be paired with distinct photodiodes to facilitate wavelength specific measurements. When the allowed wavelengths change linearly along a wedge, the wedge filter is called a linear variable filter (LVF). This gives a spatial aspect in relation to the wavelength. When used with a photodiode array, an individual pixel corresponds to specific wavelengths determined by the resolution of the LVF and the size of the pixel resulting in a simple spectrometer[19, 27]. LVFs function the best when the incoming light is perpendicular to the surface of the filter.

After passing though tissue, outgoing light is highly diffuse[10]. This is a challenge for interference-based spectrometers, as the light is no longer perpendicular to the surface of the filter allowing unwanted light to pass through[28]. A collimator could be used to collimate the light prior to the spectrometer but, lens- or aperture-based collimators require long optical pathlengths, making them non-ideal for miniaturized devices. One solution to this issue is to utilize parallel hole filters, a type of collimator that can miniaturize. With the use of carbon nanotubes (CNT), we made a miniaturized collimator idealized for spectrometer-based wearable optical health monitoring[29].

1.5 Parallel Hole Collimators

Commonly optical collimation is performed on light emitting from a singular source, making lenses and mirrors good collimators. But with tissue measurement the outbound light is highly diffuse and must be collimated by holes and long pathlengths. Alternatively, collimation can be performed using a parallel hole collimator (Figure 1). These collimators work by only allowing light through within a set on angles dictated by the height and hole size of the collimator[30-32](Figure 1 left). They also require the material the collimator is made out of to be highly absorptive to light. Any light that hits the sidewalls is absorbed only allowing the collimated light to pass through (Figure 1 left). The throughput through the collimator will be directly related to the amount of collimation. The more collimation the less light will pass through the collimator.

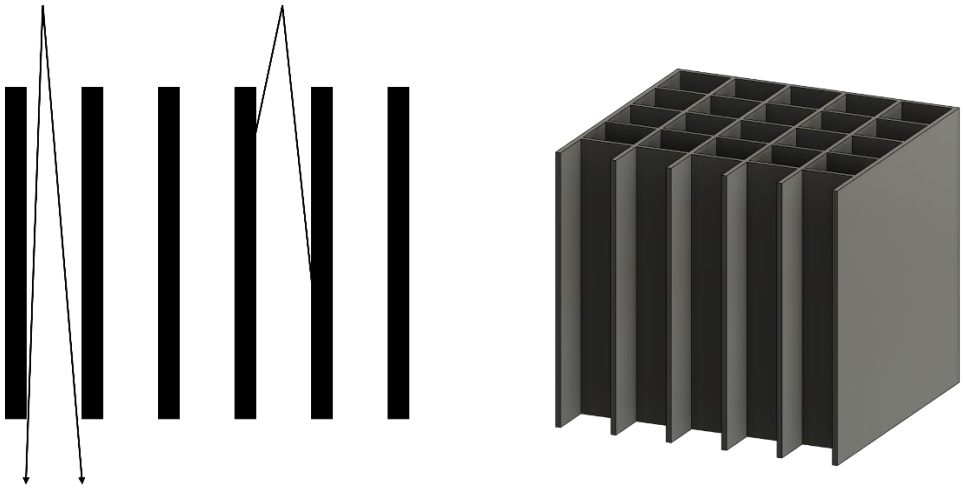

Figure 1) *Parallel hole collimator Left) A side view of a parallel hole collimator. Light that is within an allowance angle is able to pass through the collimator. Any light outside the allowance angle hits a sidewall and is absorbed. Right) A 3D rendering with a cut out of a parallel hole collimator.*

1.6 Carbon nanotubes CNT-M

Carbon Nanotubes (CNTs) are a unique material that can be patterned into 2D and 3D structures. Rather than silicon microfabrication which generally requires the removal of material,

CNTs grow from photolithographically patterned iron (Figure 2 top). This allows for precise placement of CNTs in controllable, configurable patterns[33]. Using iron as a catalyst, and chemical vapor deposition of carbon, vertical CNT structures are grown matching the deposited iron pattern. This allows for the fabrication of high aspect ratio 3D structures[34, 35]. CNTs can be grown in vertically aligned forest to make CNT micro electromechanical devices[36, 37].

As grown, CNTs are fragile and difficult to handle, making their use in applications that involve regular handling or direct contact difficult. A common way to increase strength and durability is through infiltration. Infiltration is the process where material is added to the individual CNTs increasing their diameter (Figure 2 bottom). The infiltration step also increases the stress between the CNTs and the substrate making removal of the CNT structure feasible.

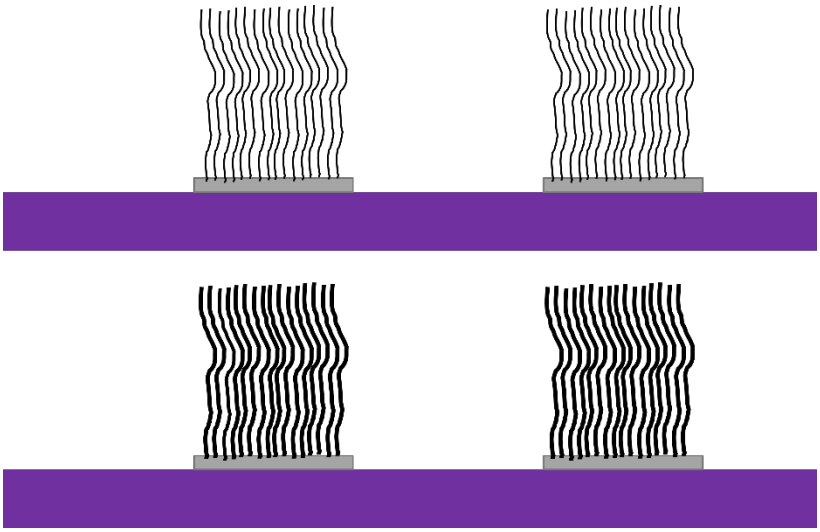

Figure 2) *Patterned carbon nanotube growth and infiltration. Top) Photolithographically patterned iron is deposited on a silicon substrate, from which vertically aligned carbon nanotubes are grown. Bottom) Carbon infiltration adds carbon to the CNTs increasing their diameter.*

1.7 Ultra-black CNTs

CNTs have also found applications in making ultra-black materials[38-41], materials with very low reflections. Due to the high absorptivity of carbon and the low density of the forest,

CNTs have been found to be one of the blackest materials made[42]. CNTs have been shown to have reflectivity down in 0.012% of red light. This low reflection can be attributed to two reasons; first the low density of carbon gives the index of reflection very close to that of air and carbon is a highly absorptive material. As infiltration increases the density of the CNTs, it also increases reflection. To use non-infiltrated CNTs (to maintain low reflectance) in a transmission application, growth would have to be done on a transparent substrate.

1.8 Overview

In this work we will show the development and characterization of a miniaturized collimator and SWIR spectrometer. Using CNT-M processes we have developed a collimator for visible and SWIR light. We will show in chapter 2 that this collimator is able to be customized to control the allowed angles of light to pass through. In chapter 3 we used this collimator design in the development of a SWIR spectrometer based on a LVF filter and linear photodiode array. The spectrometer dimensions were 14 mm x 4 mm x 3 mm. The dark current noise measured on the spectrometer with customized electronics was -28dB. This miniaturized spectrometer has a resolution of 13nm at 1300nm, while having over 100x the light sensitivity to a comparable diffraction grating based spectrometer for physiological measurements. We will show results taken on a human subject and that the spectrometer is able to measure a pulse. We have collected data using 5 LEDs with the spectrometer placed over the radial artery on the wrist. We will show the results from the 1050 nm pixel as it has the best transmission of the wavelengths illuminated and shows the clearest pulse. In chapter 4 we will show the effect of sidewall reflections on the spectrometer performance. We will show that by growing on a transparent substrate we can use non-infiltrated collimators to eliminate sidewall reflections, thus improving the quality of the spectrometer. Lastly in chapter 5 we will show how we can calibrate each spectrometer and see

unit to unit variations in assembly and collimator quality. We will show calibrations for dark current, a bright field correction and a wavelength calibration to convert the native pixel numbers to wavelengths.

Chapter 2, *Visible and short-wavelength infrared light collimation through carbon nanotube, parallel hold collimators* is the manuscript for a paper published in Optics Express. My contribution to that work was the experimental design along with the initial experimental setup. I did the majority of the CNT growth and data collection. All SEM images were taken by me. Chapter 3, *Miniaturized spectrometer for diffuse light applications* is the draft of the work being prepared for submission. My contribution to that work was construction and testing of the spectrometers, along with all the experimental designs, improvements and corrections to code made by Nick Morrill. Chapter 4 came from my discovery of the irregularity in data collected from diffuse light sources. Zack Westhoff grew the collimators while I did the experimental designs and data collection. It is hoped that this work will become the foundation for another paper. Lastly Chapter 5 will be part of the supplementary information for the paper based on chapter 3. I did all the experimental design, setup and data collection for this chapter.

Chapter 2: Visible and short-wavelength infrared light collimation through carbon nanotube, parallel hole collimators

The following is the text from a published paper in Optics Express. *Tyler Westover, Scott Olsen, Zach Westhoff, Nick Morrill, Robert Davis, and Richard Vanfleet, "Visible and short-wavelength infrared light collimation through carbon nanotube, parallel-hole collimators," Opt. Express 30, 22679-22686 (2022)*

https://doi.org/10.1364/OE.458656

Tyler Westover did the experimental design and growth of the first CNTs used along with the majority of the data collection. Tyler modified and used code developed by Richard Vanfleet for the modeling and figures. Scott improved the experimental setup and Zach did a lot of CNT growth. Nick Morrill helped with some mask design and discussions about experiments to perform. Robert Davis helped guide the work through mentoring.

Visible and short-wavelength infrared light collimation through carbon nanotube, parallel-hole collimators

Tyler Westover[1,2,*], Scott Olsen[1], Zach Westhoff[1], Nick Morrill[2], Robert Davis[1], Richard Vanfleet[1]

[1]Brigham Young University Department of Physics and Astronomy, N283 ESC, Provo, Utah, 84602, USA
[2]Tula Health Inc, 686 N Arbinger Way, Farmington, Utah, 84025, USA
**tyler.westover13@gmail.com*

Abstract

Traditional collimators typically require large optics and/or long pathlengths which makes miniaturization difficult. Carbon nanotube templated microfabrication offers a solution to pattern small 3D structures, such as parallel hole collimators. Here we present the characterization of a carbon nanotube parallel hole collimator design and its efficacy in visible and short wavelength infrared light. Comparison to geometric and far field diffraction models are shown to give a close fit, making this a promising technology for miniaturized diffuse light collimation.

2.1 Introduction

In many optical detection applications, the light of interest becomes diffuse after passing through a sample and requires some form of collimation for analysis; unfortunately, traditional collimators using lenses or multiple apertures are difficult to shrink, presenting a roadblock to the miniaturization of optical systems. However, parallel-hole collimators show promise for optical collimation and are amenable to miniaturization by using small, closely spaced holes in a relatively thin plate. When the spacing between holes is small, a sidewall material with high absorption is required for effective collimation. Previously miniaturized parallel-hole collimators have been fabricated using silicon micromachining to analyze visible light from highly scattering media.[30, 32]

Carbon composite, parallel-hole collimators formed using carbon nanotube templated microfabrication (CNT-M) offer several potential advantages over silicon-based alternatives. These advantages include the facility of precise, high-aspect-ratio fabrication[33, 43] as well as the highly absorptive nature of carbon composites in both visible and—unlike silicon—infrared wavelengths of light. Patterned, vertically aligned CNTs are extremely fragile, making them difficult to handle in processing and severely limiting the range of applications. However, CNT-M uses carbon infiltration (or other infiltration materials) to significantly improve the robustness of high-aspect-ratio CNT structures[34, 36, 37, 44] while retaining the high-fidelity patterning. The pyrolytic carbon infiltration process deposits carbon onto the surface of individual CNTs, effectively thickening them and bonding them together. After carbon infiltration, optical imaging shows that these structures are still very absorptive.[36]

In this work we used carbon-infiltrated CNT-M to form parallel hole collimators for use in the visible and near-infrared. The patterned CNTs were formed into a rectangular grid with pore sizes of 25, 50, 100 and 200 microns and heights between 100 and 880 microns. Collimation performance was determined by measuring transmission through the micro-collimators as a function of angle. Briefly, collimated light (both visible and NIR sources) was passed through the CNT micro-collimators and transmitted light was detected using either silicon or InGaAs photodetector. The collimator was tilted through various angles; at each angle the intensity at the detector was recorded. The reduction in intensity through various angles was modeled using both a basic geometric approach and one incorporating far-field diffraction effects. We have verified that CNT-M collimators perform very closely to the predicted values as modeled. The aspect ratios (collimator height divided by pore width) ranged from 1.25 to 32 with cutoff halfwidth angles (angle at which no light passes through) ranging from 3 to 38

degrees. We have also verified through modeling that some single sidewall scattering occurs and measured a detectable amount of double sidewall scattering.

2.2 Methods

CNT-M fabrication was performed as described by Fazio et al[36]. Briefly, CNT growth substrates were prepared by sputtering 50-70 nm of alumina on single-crystal silicon wafers (Figure 3A). Patterned thin film iron catalyst was then added as follows (Figure 3B). Photoresist (AZ3330, AZ Electronic Materials) was spun onto the wafers at 5000 rpm. The collimator pattern was exposed with UV light for 10 seconds. The photoresist was then developed in AZ300MIF (AZ Electronic Materials) for 45 seconds. Excess photoresist was removed by a 30 second water rinse. The wafer was then dried using a nitrogen gun. Using a thermal evaporator, 4 nm of iron was deposited onto the patterned photoresist. Liftoff of the excess iron was done by sonication of the sample in 1-methyl-2-pyrrolidone, (Sigma Aldrich) for 5 minutes. Samples were then rinsed in deionized water and dried using nitrogen. CNT growth was accomplished in a 1-inch quartz tube furnace at 750 °C. Hydrogen and ethylene were introduced at flow rates of 311 sccm and 338 sccm, respectively. Growth times varied from 2-15 minutes depending on the target growth height, after which the ethylene flow was turned off and the temperature increased to 900 °C for carbon infiltration of the CNT forest. Once the target temperature was reached, ethylene flow was reintroduced at 338 sccm for 10 minutes (Figure 3C). The tube was then cooled in argon. The sample was then removed, followed by a plasma etch (Techinics Planar Etch 2) in an oxygen plasma at 200 W in 5-minute intervals to remove the floor layer (a layer of carbon on the substrate and bottom of the CNT forest formed during infiltration). After each 5-minute interval, the chamber was vented, and the forest inspected. Once, CNT forest had

separated from the silicon substrate, the forest was flipped over, exposing the bottom, and an additional 5-minute, 200 W plasma clean was performed (Figure 3D).

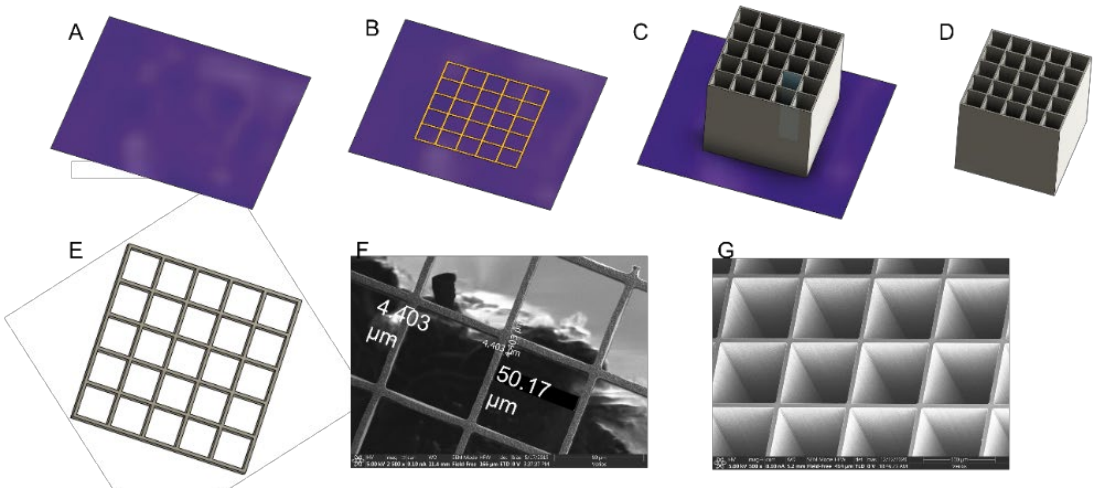

Figure 3*) CNT growth process. A) Alumina is deposited on single crystal silicon substrate B) 4nm of iron is photolithographically patterned onto the substrate C) Patterned CNTs are grown and D) CNT-M collimator is released from the substrate using plasma etch. E) Top down view of the collimator showing the square pores and the open channel. F) SEM image of the top view of the collimator showing the tops of the walls and the open channel. G) Angled SEM image of a collimator showing the walls and square channel.*

Sample heights were measured using an optical microscope (Olympus BX60, Olympus UMPlanFl 20x lens). Focusing on the top and the bottom of the CNT forest allowed for the determination of height with the stage height dial; this method for height measurements has an approximate error of 10-20µm as compared to a calibrated SEM measurements on the same sample. To minimize errors due to backlash in the optical microscope mechanical stage, measurements were performed moving only downward until the top of the collimator is in focus, pausing to record the position at the top, then continuing only downward until the bottom of the collimator is in focus and the bottom position is recorded. To verify heights and determine lateral dimensions of the pore size and wall thickness, a few collimators were characterized by scanning electron microscopy using a Verios G4 SEM.

The infiltrated CNT collimators were mounted onto 33mm OD, 13mm ID washers using gel superglue on the corners for optical testing. The washer was then inserted into an optical mount on a rotation stage. The optical test setup is diagramed in figure 4. A laser at the source position was used for alignment of optical elements: lens, aperture, collimator, and detector. LEDs of desired wavelengths (red - 650 nm or IR - 1550 nm) were used. The light from the LED was collimated by adjusting the distance between the LED and the lens (focal length 50mm, diameter 25mm). The aperture was adjustable and set to a 1mm opening for 660 nm and 1cm opening for 1550 nm. The distance between the CNT collimator and the photodetector (Si with 4.4 mm x 4.4 mm effective area, InGaAs with 1 mm x 1 mm effective area) was ~125mm. The collimation of the beam was determined using a setup containing only the LED and the lens, by measuring the beam size at the lens (25 mm diameter beam) exit and again at 60 cm past the lens. There was no more than a ~2 mm change in beam size over the 60cm distance giving a collimation of ~0.3 degrees. The beam reference intensity was recorded with the collimator removed and a dark level was recorded with the beam blocked. Zero tilt incidence, in reference to the LED, was found by rotating the collimator until the maximum intensity was recorded on the detector. As the collimator is tilted, the reduction in intensity is due to the size of the direct optical path being decreased, until it is completely cut off, represented schematically in figures 4B-D. The intensity of the light at the photodetector was recorded at varying angles.

The above experimental description includes variation and measurement of only one tilt axis. The collimator is a 2-dimensional array with a degree of alignment determined by two tilt axis angles. The second tilt axis and rotation about the beam direction were not explicitly varied.

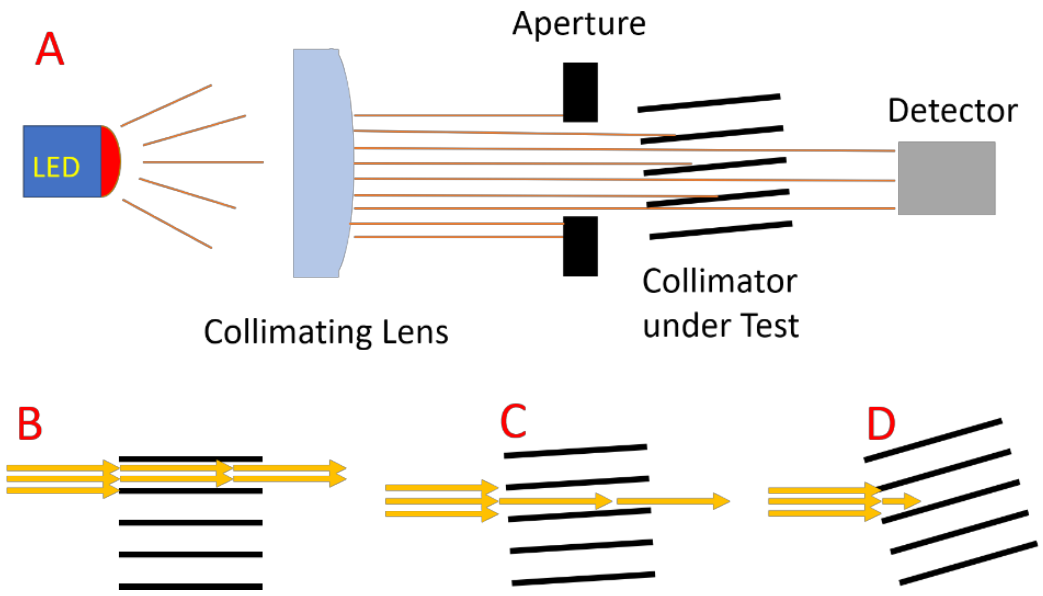

Figure 4) *Illustration of the optical test setup and process. A) A LED was collimated using a lens and an aperture, which then passed through a collimator and was collected at the detector B) A large portion of the light passes through when it is perpendicular to the collimator surface C) As the collimator is tilted light is partially blocked illustrating the reduced transmission off-angle light D) As the angle is increased beyond a cut-off point, there is no straight path for light through the collimator.*

While mounting the collimator on the washer, and the washer in the optical mount, effort was made to align the second tilt axis and to align the array directions with the tilt axes. Any offset in the second tilt direction will decrease the peak transmission, but subsequent tilt variation of the primary tilt direction should still be linear.

Collimators with pore sizes of 25, 50, 100 and 200 microns were studied. The collimators were grown to varying heights ranging from 100 to 880 microns to test various aspect ratios. In this work the aspect ratio is defined as the height of the collimator divided by the pore size (h/d). Red (650 nm) and IR (1550 nm) LEDs were used to illustrate the visible and IR ranges. For red light the detector was 4.4 mm x 4.4 mm for IR sources, the available detectors are small (1 mm x 1mm) and an integrating sphere with an 11.2 mm diameter entrance size was used to collect

more light, increasing our signal to noise. The location of the collection port of the sphere reduced the optical pathlength from 125 mm to 90mm.

2.3 Results and discussion

Optical transmission measurements were measured for collimators with square pores with dimensions of 25 x 25 µm, 50 x 50 µm, 100 x 100 µm and 200 x 200 µm. Transmission was measured for angles ranging from normal incidence to well beyond the cut off angle of each collimator as illustrated in figures 4B-D. Applying a strictly geometric model, the intensity of the light should decrease linearly as the collimator is tilted toward the optical axis ($I = I_o(1 - \frac{h}{d}\tan(\theta))$). The angle at which the light is completely cut off is then the Arctangent of the pore size divided by the height of the collimator, i.e., the $\tan^{-1}(\frac{d}{h})$. Figure 5 shows measured transmission data and model calculations using 650 nm light for a representative low aspect ratio (Figure 5A) and high-aspect-ratio (Figure 5B) collimator as well as the measured and modeled cutoff angle vs aspect ratio (Figure 5C) (Supplementary Dataset 1[29]). The model curves in figures 5A and 5B are not fits to the data but were calculated using measured properties such as height, pore size, beam width and detector size(Supplementary Code 1[29]). In addition to the 10-20 µm uncertainty in the height measurement, there is a variance in height across the sample that can be as much as 10-15% of the height. Allowing some error in these geometric quantities, the simple geometric model has a reasonable match to the data. However, transmission measurements for the lower aspect ratio collimator (1.25 ratio for Figure 5A) were found to decrease with tilt faster than the 250 µm tall model would predict, but matches a 275 µm tall collimator shown in the green dotted line. The 275 µm height falls within the height measurement uncertainty in these samples. The addition of far field diffraction to the model

slightly decreases the transmission at larger incident angles, although this change is small compared to the impact of height uncertainty A far field diffraction model was used due to the distance between the collimator and the detector (9-12.5 cm) being large compared to the wavelength. The model is based on an array of simple slits that decreases in projected width with tilt, assuming total absorption by the sidewalls. In this model, the diffraction effects broaden the distribution at the detector sending intensity beyond the detector edges. Higher order diffraction

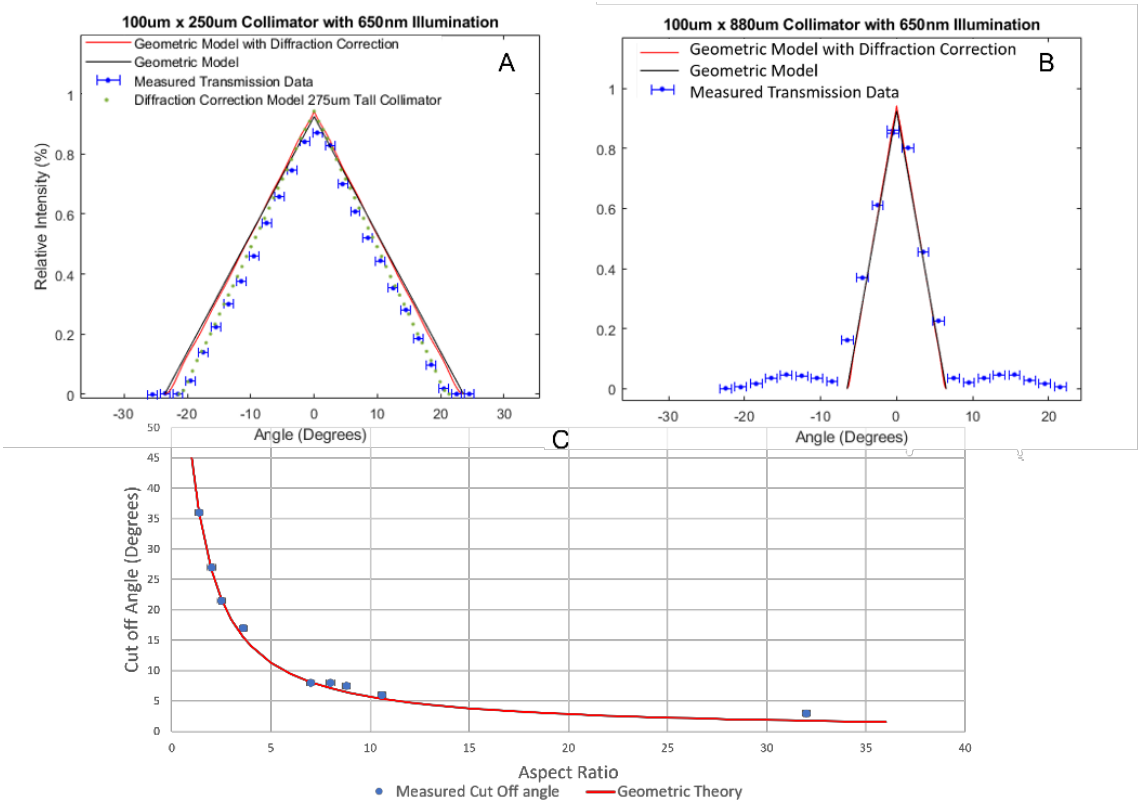

Figure 5*) Collected intensity data vs angle for visible light compared to the model. Shown are data sets collected for two different collimator geometries. A) Transmission through a low aspect ratio (1:2.5) collimator(Pore size: 100 µm, Height: 250 µm) resulting in large angles of light being able to make it through. Because of the uncertainty in the collimator height measurement, an additional model prediction (shown as green dots) for a height of 275µm is included. B) Transmission through a high-aspect-ratio (1:8.8) collimator(Pore size: 100 µm, Height: 880 µm) resulting in only small angles allowing light to pass. C) Collimation cut off angle vs. collimator aspect ratio. The line shows the prediction from geometric theory shown in figure 2 plotted with measured cut off angle values. Aspect ratios range from 1.25 to 32.*

peaks extending past the edge of the detector can be seen by eye, supporting the model premise (Supplementary Visualization 1[29]). The largest effect would be seen if only the main transmission peak was included in the detector. The detector size includes most of the diffraction peaks, making the diffraction correction relatively small. However, the lower transmission at high tilt angles will become more prominent for low aspect ratio collimators and at larger collimator to detector separations due to the decreasing effective slit width placing more intensity beyond the detector. This effect is much smaller in higher aspect ratio collimators due to fewer datapoints in the tilt range and is also minimal in the IR data due to the detector size collecting more diffraction peaks than in the visible. At non-normal incidence some shallow angle light will be reflected off the sidewalls and hit the detector due the detector's size and proximity to the collimator. Light reflected off a single wall may contribute to the detected signal but, must have an angle less than ~2 degrees (~7 degrees) to hit the detector for 660nm (1550 nm). Both geometric and diffraction corrected models were used to predict transmission only up to the cut off angle.

Figure 5b shows a high-aspect-ratio collimator in comparison to geometric and diffraction corrected models. In addition to the expected linear drop-off of intensity, the high-aspect-ratio collimator exhibited small broad peaks in intensity centered at ± 14 degrees from normal incidence, approximately twice the geometrically expected cut-off angle. We hypothesize that these peaks are due to double reflections off the walls of the infiltrated CNTs pores, which are not as absorbent as as-grown CNTs. Observed intensity must reach the detector on the optic axis of the experiment, eliminating the possibility of single wall reflections and higher order diffraction peaks. Other than at very small angles, light reflected off a single wall (or an odd number of walls) will miss the detector by exiting the collimator at an angle of 2Θ, but light

reflecting off two walls (or an even number of walls) will return to the optic axis and be collected. This two-reflection light will be minimum at the critical tilt and maximum at twice the cut-off angle, consequently larger angle two-reflection light will not contribute to the measured intensity below the cut-off angle. We expect that these double reflection peaks to be seen in the low aspect ratio data but due to the limited scan range of collimator angles it is not seen in our low aspect ratio data.

Measured cut off angles for collimators with pore sizes of 25, 50, 100, 200 μm and heights from 100 μm to 880 μm are shown in figure 5C as a function of the aspect ratio with the solid line showing the predicted cut off angle from the geometric model. The collimator cut-off value matches closely to that predicted by the geometric model.

The transmission experiments were also performed using collimated IR (1550 nm) light with data shown in figure 6 (Supplementary Dataset 2[29]). There were some challenges when working with IR LEDs and InGaAs devices that required some setup modifications. Due to the lower efficiency of IR LEDs the size of the aperture controlling the beam width had to be enlarged to get enough signal to the detector. The area of InGaAs photodetectors is typically much smaller than that of silicon photodetectors, 1 mm x 1 mm for InGaAs but 4.4 mm x 4.4 mm for Silicon. This was compensated for by using an integrating sphere to collect the total signal that passed through the collimator and enters the larger entrance aperture with a 11.4 mm diameter. This larger diameter aperture allows for an even larger portion of the diffraction peaks to be detected, making the diffraction model almost match the geometric model. Figure 6A and 6B show the IR results vs tilt angle for the same collimators as in figure 5A and 5B. As in figure 5, the models shown are not fits to the data, but calculations based on the measured or defined geometries of the collimators.

The data is these measurements fit closely to the geometric model due to the large detection area due to the opening of the integrating sphere collecting more of the diffraction peaks. The size of the integrating sphere also brings the detector closer to the collimator, also allowing for more diffraction peaks to be collected. The small double reflection effects are also visible in the high-aspect-ratio IR data. Figure 6c shows the measured IR cutoff angles and the predictions of the geometric model. Due to the lower efficiency of IR LEDs the beam size was expanded to allow more light at the detector, this resulted in some of the smaller collimators not

being used in for the IR trials, as they were smaller than the beam size. Thus, there are fewer data points in 4C than the corresponding data in 3C.

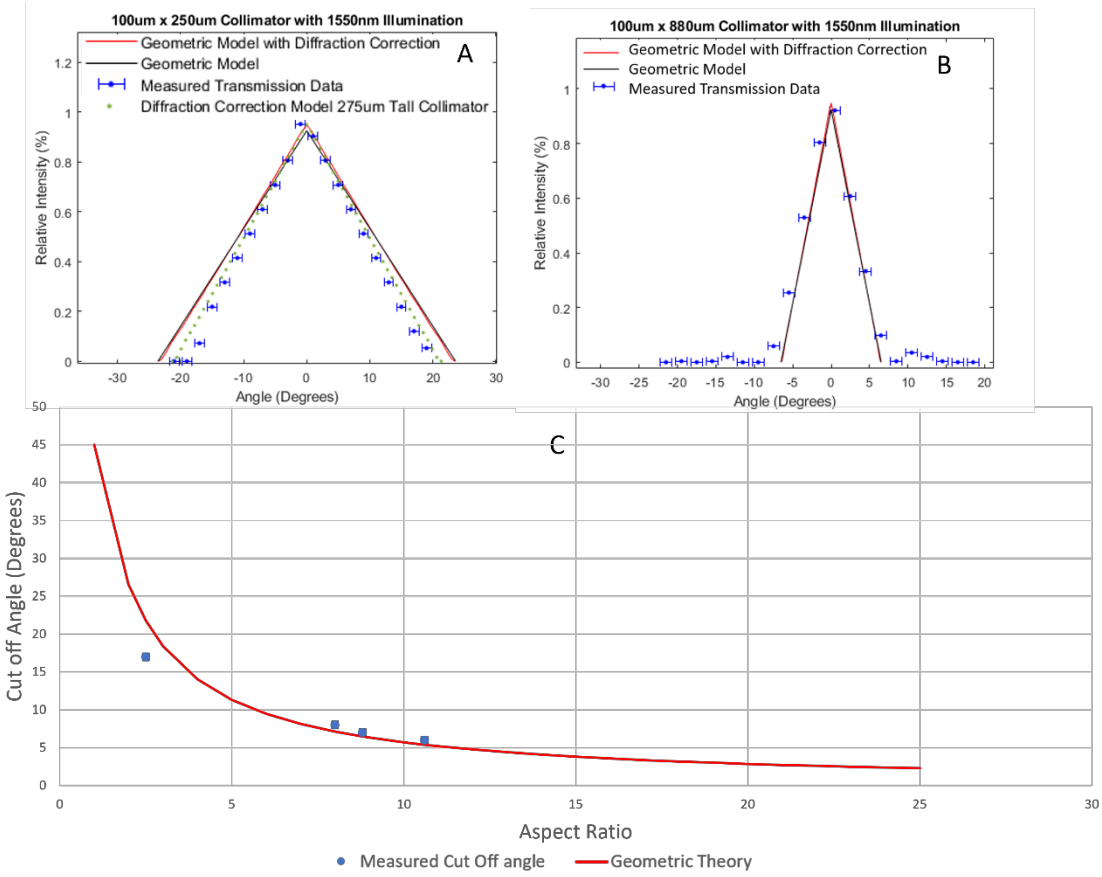

Figure 6) *Data sets of collected intensity data vs angle for IR light compared to the model. Shown are data sets collected for two different collimator geometries. A) A low aspect ratio (1:1.25) collimator resulting in large angles of light being able to make it through. Because of the uncertainty in the collimator height measurement, an additional model prediction (shown as green dots) for a height of 275µm is included. B) A high aspect ratio (1:8.8) collimator, resulting in only small angles allowing light to pass. C) Collimation cut off angle vs collimator aspect ratio plotted over a similar range as figure 5 for easy comparison. The line shows the prediction from geometric theory shown in figure 4 plotted with measured cut off angle values. Aspect ratios range from 2 to 10.*

2.4 Conclusions

We have demonstrated the effective miniaturization of a collimator based on patterned CNTs. We have shown that with photolithographic patterning we can design a CNT forest in a

simple grid pattern. This grid pattern was infiltrated for strength and the resulting material was found to be absorptive of visible and IR light. We showed that this collimator is effective at collimating light in both the visible and near infrared portions of the spectrum. Using a simple geometric model with added far field diffraction effects to calculate transmission we found a correlation between theory and experiment. Although relatively small, double wall reflections were observed. Sidewall reflections of CNT collimators from both one and two walls could be significant to performance in some applications and would be beneficial to study in future work. Improvements to reduce sidewall reflections could involve minimizing infiltration time at the expense of strength/handleability or the use of different infiltration materials to maximize absorptivity.

Acknowledgements**:**

This research was partially supported and funded through Tula Health Inc.

We would like to thank the BYU microscopy and cleanroom facilities for their support.

Funding:

This research was supported and funded through Tula Health Inc and Brigham Young University

Disclosures**:**

T. Westover: Tula Health Inc (F,E,I), Z. Westhoff: Tula Health Inc (F,E), N. Morrill: Tula Health Inc (F,E,I), R.Davis: Tula Health Inc (F,I,P), R. Vanfleet: Tula Health Inc (F,I,P)

S. Olsen declares no conflict exists

Chapter 3: Miniaturized spectrometer for diffuse light applications

This work is being prepared for submission.

In this work Tyler Westover did the assembly of the spectrometers, modification of the code originally written by Nick Morrill for the model, the experimental design and the data collection of single spectrums and on human subjects. Zach Weshtoff did temperature-controlled data runs. Sharisse Poff and Shiuh-hua Wood Chiang did the development of the teensy based interface board. Nick Morrill helped with the original collimator mask design and some early testing and wrote the code for the model. David Miller, Robert Davis and Richard Vanfleet mentored throughout the process.

Miniaturized SWIR Spectrometer for Diffuse Light Applications

Tyler Westover, Zachary Westhoff, Sharisse Poff, Nick Morrill, David Miller, Shiuh-hua Wood Chiang, Richard Vanfleet, Robert Davis

Abstract: A miniaturized short-wavelength infrared spectrometer was realized by combining: a thin form factor carbon nanotube composite collimator, a linear variable filter and an InGaAs photodiode array. The resultant spectrometer is 3 x 4 x 14 mm in size and with diffuse light shows a significant improvement in resolution over the spectrometer without the collimator. The small size and high throughput could be enabling in wearable optical sensing where light is highly diffuse. Plethysmographic measurements on the wrist were demonstrated, showing rapid data collection with highly diffuse light.

3.1 Introduction

Recent advancements in tissue measurements have allowed for the widespread use of wearable health monitors. These health monitors incorporate sensors to obtain and report a wearer's physiological data with the goal of enabling more informed health decisions. Additional physiological information can be obtained with more versatile miniature sensors[1, 8]. One region of the optical spectrum with untapped potential for continuous measurement of physiological information is the short wavelength infrared (SWIR)[10, 11]. The SWIR region of the infrared typically incorporates 900-1700 nm light. In this region there are key absorption peaks for biological molecules, including glucose, urea, triacetin and water[10, 12, 13]. Changes in the peaks cannot easily be isolated using traditional broad LEDs and a single photodiode, thus causing

them to become confounding variables for one another. This presents the need for higher resolution data, a challenge that may be helped by a miniaturized spectrometer.

Spectroscopy is an invaluable tool in better understanding materials and the chemical makeup of matter[15] including those relevant to health such as physiological concentrations of molecules. Recent research has focused on both miniaturizing and reducing the cost of spectrometers, increasing their availability and utility[16, 17]. Spectrometers use one of several methods to separate the light into composite wavelengths, including: diffraction gratings[18], wedge filters[19], Fourier transform[20], and tunable filters[21]. Each technique requires collimated light for optimal performance. Wedge filter-based spectrometers have been studied as one route to spectrometer miniaturization[19, 25, 26, 45]. Wedge filter-based spectrometers operate on the same principle as interference band pass filters, i.e., thin film deposition that allows only a narrow set of wavelengths of light through a given area. However, in a wedge filter, the interference layer thickness is varied from one side to the other across the filter, resulting in the passband center wavelength varying with position. When the allowed wavelengths change linearly along the wedge, the wedge filter is called a linear variable filter (LVF). When combined with a linear photodiode array, an individual pixel corresponds to specific wavelengths resulting in a simple spectrometer[19, 27].

LVFs function the best when the incoming light is collimated perpendicular to the surface of the filter. However, after passing through tissue, outgoing light is highly diffuse[10]. This is a challenge for LVF-based spectrometers as the light is no longer perpendicular to the surface of the filter, thus allowing unwanted light to pass through[28]. A collimator could be used to collimate the light prior to the spectrometer, but traditional lens- or aperture-based collimators require long optical pathlengths, making them non-ideal for miniaturized devices. One solution to this issue is

to utilize parallel hole filters, a type of collimator that can be miniaturized. With the aid of carbon nanotube templated microfabrication (CNT), we recently designed, fabricated and tested a miniaturized collimator intended for spectrometer-based wearable optical monitoring[29].

In this work we present the design and characterization of a miniaturized SWIR spectrometer for diffuse light applications. The spectrometer consists of a CNT collimator, an LVF, and a 128 pixel linear photodetector array (figure 7). The resulting resolution (Full width half max-FWHM) of 13 nm @1300 nm and the collimating characteristics are compared to an analytical optical model. The dark current noise was measured to be -28dB. Additional calibrations including dark current subtraction and bright field correction were done and discussed in chapter 4. In a human subject experiment the sensitivity was compared to a commercially available Ocean Insight grating-based spectrometer and found to have a throughput of more than 100x higher than the grating spectrometer. Using surface mount LEDs illumination, the spectrometer was used to demonstrate collection of high quality plethysmographic signals from the radial artery of the wrist.

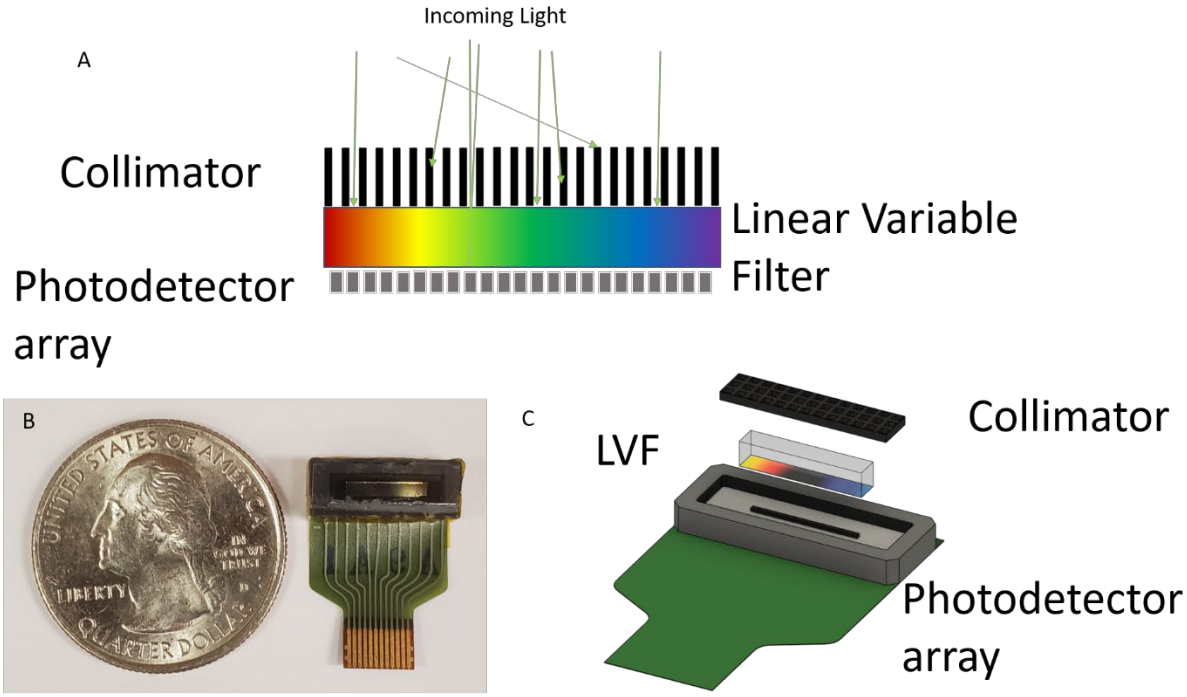

Figure 7) *Schematic view of the spectrometer assembly. A) Monochromatic diffuse light enters spectrometer from the top. The light is collimated by the CNT collimator, separated by wavelength by the LVF and ultimately collected by the photodetector array. Compete spectrometer (B) compared in size to a quarter. A 3D printed holder contains the linear variable filter and collimator and is sealed with a plastic window. The Photodiode array is attached to a flexible substrate. Full spectrometer is compared to the size of a quarter. C) CAD illistration of the collimator, LVF and Photodiode array. This exploded view shows the components without the 3D printed holder.*

3.2.1 Materials and Methods

The carbon nanotube collimator was made as described previously[29]. Briefly: 70 nm of alumina was reactively sputter coated onto silicon substrates. Then, a CNT growth catalyst (4 nm of iron) was deposition in a pattern onto the substrate using contact lithography, thermal iron evaporation and liftoff. Carbon nanotube forest growth from ethylene gas was then performed in a one-inch tube furnace at 750 °C. The growth time was 6 minutes to result in the desired CNT growth height of 400 µm. Following growth, the CNT forest was infiltrated with carbon (10 minutes in ethylene at 900 °C) to improve the strength of the CNT collimator. After growth and

infiltration, the samples were exposed to an oxygen plasma for 10 minutes to remove excess carbon deposited on the substrate during infiltration (the plasma releases the collimator from the substrate).

The linear variable filters were purchased from Viavi Solutions (900-1650 nm wavelength range). The photodiode arrays were purchased from Hamamatsu (G13913-128FB). All single spectrum data collection measurements from the Hamamatsu array were made using a development board and software provided by Hamamatsu. A 16-bit microcontroller-based (Teensy 3.5) data collection system was developed and used for longer runs and pulsatile data collection and was described previously[46]**.**The collimator housings were designed using computer-aided design software (CAD) and 3D printed on the Formlabs Form 3 stereolithography printer using Formlabs standard black resin (CAD model in figure 31 and 32). To cover and protect the collimator during spectrometer handling, a thin glass or plastic slide was cut and attached to the collimator housing using super glue. A CAD model of the assembly is shown in figure 7C (for illustration the housing is not shown).

The spectrometer was built to have dimensions of 14 mm x 4 mm x 3 mm. Figure 7B shows the spectrometer in respect to a U.S. quarter. In this configuration a large amount of the size is attributed to the flexible PCB, which was used for ease of testing, but is not required, as the spectrometer can be directly mounted to a printed circuit board (PCB). An exploded CAD model of the spectrometer is shown in figure 7C. Note the alignment of the three main components: the collimator, LVF and photodiode array.

To determine the resolution of the spectrometer, mono-chromated light was provided by Spectral Products (DK240) using a tungsten filament light source. The slits on the monochromator were adjusted to maximize light output while keeping a small spectral width.

The spectral width was calculated to be 2 nm based on the slit width chosen. Light exiting the monochromator was diffused using a diffusing mirror (Thorlabs DG10-1500) reflected onto an 100 degree engineered diffuser that was placed directly on the spectrometer (figure 8B). Diffused light illuminated the full spectrometer, and the full width half max (FWHM) of the beam was measured. This was repeated with reported center wavelengths every 100 nm starting at 1000 nm and ending at 1500 nm. Measurements were taken both with and without the collimator to determine the effect of the collimator on the spectral resolution and overall performance. The monochromatic light was dim and required an integration time of 0.5 s to get a clear signal over the noise. Dark noise was collected by taking a spectrum when the illuminating light source was off. This was subtracted from the spectrum collected with the light on to determine the resolution of the spectrometer. Wavelength calibration was done by using the reported monochromator center wavelengths to map the photodetector pixels to a wavelength. For the pixels between

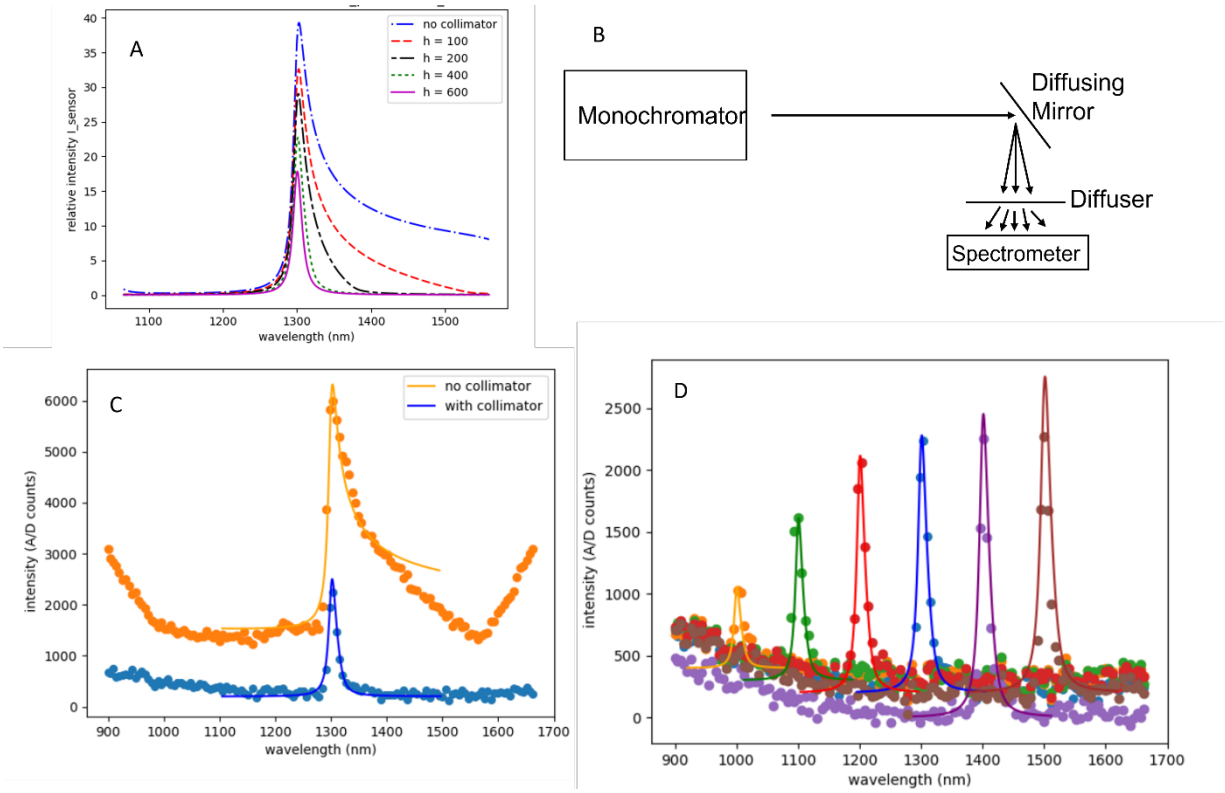

Figure 8). *Mono-chromated light exits the monochromator and is diffused first by a reflective diffuser and second by an engineered diffuser that is immediately above the spectrometer. Data is collected with and without the collimator. A) Modeled intensity distribution from the LVF-Photodiode combination with 100 µm pore with 5 µm sidewalls and varying heights in µm. B) Schematic of the experimental setup. C) Spectrum of light taken by the spectrometer from monochromatic diffuse light with center wavelength at 1300 nm and a FWHM of 2 nm with a CNT collimator (orange dots) and without (blue dots). The model in A is fit in amplitude and baseline to the data(solid line). D) Diffuse light shone into the spectrometer at different wavelengths(dots) and the spectral response is plotted. At 1300nm the FWHM is about 13nm, matching the expected resolution of the LVF(Lines).*

peaks, interpolated values of wavelength were used. Alternatively, a krypton spectral calibration lamp can be used to calibrate the spectrometer as described in chapter 4.

To characterize dark noise, dark current was measured in a temperature-controlled chamber for 20+ hours. The charge from each pixel was converted to a voltage and all 128 pixels were recorded every 10 ms by the microcontroller. The 10 ms cycle time consisted of an 8.5ms charge integration time and a 1.5 ms data readout time for the 128 pixels. In chapter 4, collected

data for a single pixel is plotted, noise in the dark current quantified and additional bright field and dark current corrections are measured.

The temperature dependence of the spectrometer dark current signal is found in chapter 4. To determine this, the chamber temperature was varied in a controlled manner in the range of 0-40°C while collecting data with the non-illuminated spectrometer. This yielded a change of up to 1000 ADC counts which is significantly larger than the dark current noise of 6 ADC counts (-28 dB).

3.2.2 Human Subjects Measurements

A human subject wrist-based test was performed to compare the throughput of our spectrometer to a commercially available Ocean Insight (Flame NIR) spectrometer. The flame was connected to a 3-ft fiber optic cable and placed on the wrist on one side of the radial artery, while a fiber optic cable from a 100-Watt adjustable tungsten bulb was placed on the other side of the artery. The artery was chosen as a candidate for the location for a wearable device. A spectrum was collected using the Flame's automatic integration feature until it settled at an integration time of 5500 ms. The Flame was then replaced by our spectrometer and the experiment was repeated using an integration time of 35 ms to yield a similar voltage at a given pixel.

Pulsatile measurements were performed using the spectrometer with LEDs (Marktech 1206 SMDs) together in a single unit. The LEDs were placed close to the expected pass-through location on the LVF. The LEDs on the board emitted light at 1050 nm, 1300 nm, 1550 nm and two at 1650 nm. The LEDs were approximately 4 mm away from the edge of the spectrometer.

The spectrometer was placed on the wrist with the detector directly above the radial artery. The LEDs were placed on the tendon side of the wrist. Data collection was performed using the microcontroller based system. The integration time was 8.5 ms with a cycle time of 10 ms. Data was collected for approximately 3 minutes.

3.3 Theory

Linear variable filters can be modeled as a series of Fabry-Perot filters. Fabry-Perot filters are thin film interference filters used to isolate a narrow band of wavelengths of light. The wavelength band is dictated by the space between two of the thin films creating a resonant cavity for harmonic wavelengths to pass through. These filters are designed for collimated light. When diffuse light is used, the filter loses efficacy, allowing a much larger band of light through (Figure 8A) as the angles changes, the pathlength of light changes, allowing for additional wavelengths to pass. A CNT collimator before the LVF limits the higher angle incident light and thus controls the size of the band of allowed light. Figure 8A shows the effect of a 100-μm wide collimator pore with varying heights.

The model shown in figure 8A has three main components: the normal incidence transmission through the filter (Equation 1), the effective change in wavelength of angled light (Equation 2) and the limiting of angles by the collimator based on aspect ratio (Equation 3). For simplicity, we model the LVF as a double boundary and a known thickness, with the assumption that the angle does not exceed the critical angle where light would be totally reflected. Random unpolarized light for the illumination with a distribution of ±50° is assumed. Transmission through a Fabry-Pérot filter at normal incidence given in Equation 1[47].

$$T^{tot} = \frac{T^{max}}{1+F\ \sin^2\frac{\vartheta}{2}} \quad (1)$$

$$\vartheta = \frac{4\pi\, nfilter\, d}{\lambda_{vac}}$$

T^{Tot} is the total light transmitted through the filter, T^{max} is the max transmission possible by the filter (50%), F is the finesse coefficient calculated it based on the specifications given of the filter of a FWHM of about 1%, yielding a value of ~1000. n_{filter} is the index of refraction of the filter, while not provided by the manufacturer it was assumed to be 1.33. d is the thickness of the cavity in the filter (distance between thin films). λ_{vac} is the wavelength of light incident on the filter in a vacuum. This equation assumes normal incidence transmission. The index of refraction and thickness of the cavity are a half integer multiples of the expected pass-through wavelength (n_{filter} d). In practice, LVFs include additional step filters to block wavelengths that are nearby half integer multiples of the passthrough wavelength. For simplicity, these multiples are ignored in this model with the wavelengths graphed limited to not show them.

Off-normal incident light is able to pass through the at higher wavelengths. Equation 2 accounts for this in the model. Equation 2 maps the higher expected filter pass through wavelength λ_{center} at incident angle θ_{in} to a new pass through wavelength λ_{eff}. The new λ_{eff} is used to replace (n_{filter} d) in equation 1 to calculate the new transmission.

$$\lambda_{eff} = \lambda_{center}(1 - \frac{1}{n_{filter}}\sin^2(\theta_{in}))^{1/2} \qquad (2)$$

The collimator has two additional impacts on the model. First is the shadowing loss due to decrease in open area. I.e., the collimator walls block part of the light even at normal incidence. The second is the limitation of allowable angles that can pass through the collimator. This is determined by equation 3. The taller the collimator for a given pore size the more limited the allowed angles that can enter the LVF.

$$\theta = ArcTan[\frac{poresize}{height}] \quad (3)$$

3.4 Results

The spectral resolution of the spectrometer was measured with diffuse light to simulate the high level of scattering that occurs when measuring bodily tissue. These tests, performed with and without collimation, show the collimator's effect on the spectral resolution. The collected spectrum shown in figure 8C is from illumination by a narrow wavelength light source centered at 1300 nm and diffused prior to detection by the spectrometer. The data was first collected without a collimator in place (plotted in orange dots). The collimator is then added to the spectrometer and the spectrum measured again (plotted in blue dots). The theoretical measurements are added to show the comparison between data and theory. The amplitude and baseline offset for the model were fit to match that of the measured data(Lines). Both measured data sets exhibit the same features as the model; there is a sharp peak at the center wavelength and a right-sided tail without a collimator. The baseline of the result without a collimator is much higher than that of the collimator measurements and the theoretical model. The measured no collimator results also have peaks at the edges of the spectrum, not shown in the model. With the collimator in place, the resolution of the spectrometer matches that of the LVF manufacturer specified 1% or 13 nm at 1300 nm.

The center wavelength was varied in 100 nm intervals from 1000 nm to 1500 nm and the resulting collimated spectra are shown as dots in figure 8D. The theoretical model is plotted in solid lines. The amplitude and baseline offset of the model were fit to match the data. The resolution of the spectrometer was measured by determining the FWHM when the spectrometer had the collimator in place (figure 8D). The results shown in figure 8D are after a dark current

subtraction. The data for the longer wavelengths 1200-1500 nm are close to the maximum intensity at 1300 nm. Each has a similar resolutions of about 1% of the center wavelength. The measured intensities of the 1000 nm and 1100 nm peaks are lower than those of the longer wavelengths. The baseline signals of the measurements all seem to increase near the 900 nm side of the spectrometer, which may be due to a small light leak on that side of the LVF.

A wearable test was performed using our spectrometer in comparison to the commercially available Ocean Insight Flame spectrometer. The spectrum of light for the two spectrometers, when illuminated on the wrist, was collected at different integration times to show the differences in throughput in a wearable application. The resulting data are shown in figure 9. To get the same A/D counts as measured on both spectrometers, the Ocean Insight Flame had an integration time of 5500 ms while our miniaturized spectrometer had an integration time of 35 ms. The Flame spectrum is significantly noisier possibly due to the long integration time. No bright or dark field corrections are applied to the miniaturized spectrometer. Although illuminated with a broad light source, both spectra have a large peak at about 1050 nm and a second small peak at about 1300 nm. In the miniaturized spectrometer there appears to be a peak developing out at 1650 nm.

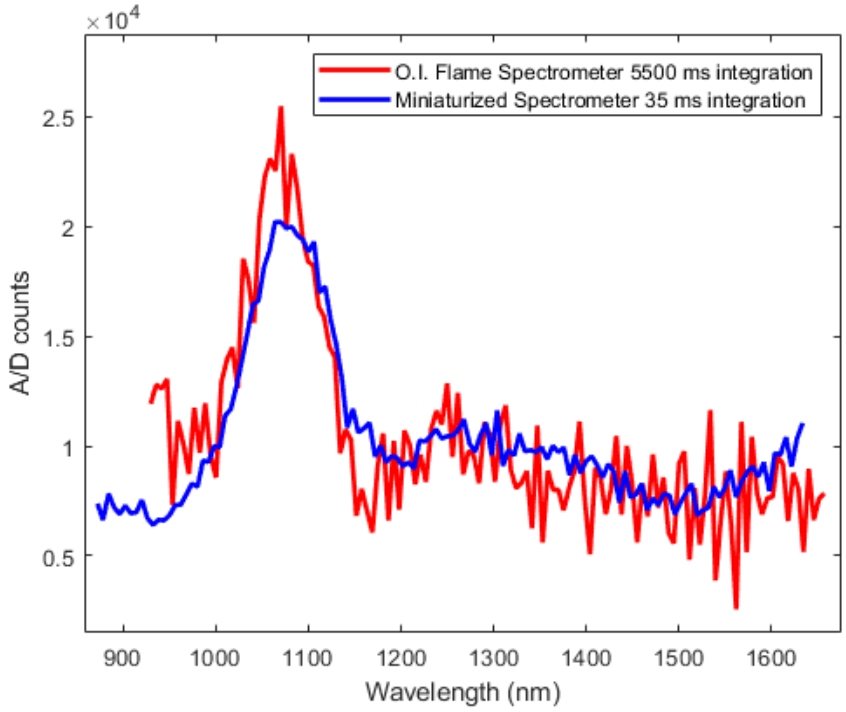

Figure 9). *Spectrum measured on the wrist with both the Ocean Insight Flame and our miniaturized spectrometer*

Measurements were taken on the wrist with the spectrometer placed over the radial artery and the LEDs on the tendon side on the wrist (Figure 10). An LED board was glued to the 3D printed housing of the spectrometer. A wrist strap shown in figure 10 was used to hold the spectrometer in place. Cables for the spectrometer and LEDs came out the side of the spectrometer module. Data was collected using the microcontroller for several minutes. A segment of that data, for the 1050 nm pixel, is shown in figure 10. The pulsatile variation in the data shown sits on the 51,000-count background shown in the vertical scale.

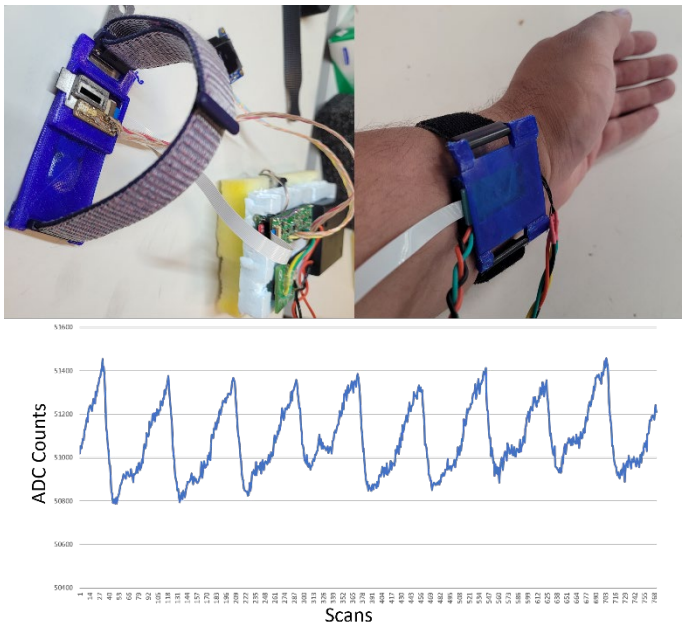

Figure 10) *A pulse measured on the wrist. Top Left) Photo of the spectrometer used on the wrist. Top Right) The spectrometer was placed directly over the artery with the LEDs placed on the tendon side of the arm. Bottom) A series of spectra were collected at 10ms intervals and the 1050nm pixel was plotted in time, yielding a pulsatile waveform.*

3.5 Discussion

The advantages of a collimator, in diffuse light measurements, for LVF based spectrometers have been demonstrated both theoretically and experimentally (Figure 8). The CNT parallel hole collimator was chosen for the collimating optics due to its ability to be miniaturized. The hole size and height of the collimator dictates the allowed angles of light that can pass through unhindered. The preferential sidedness of the light exhibited by the filter is characteristic of these types of Fabry-Perot bandpass filters when illuminated with off-normal incidence light as seen in figure 8C. As light of a fixed wavelength passes through the filter at an angle, it is able to pass through the collimator at a location corresponding to a longer wavelength. To prevent incorrect spectral measurements, a collimator is required to limit the allowed angles

of light into the LVF. A key takeaway from the model is the tradeoff between resolution and throughput; the inclusion of a collimator can shrink the FWHM of the allowed light through the LVF at the cost of total signal. As mentioned, the no-collimator measurements have a higher baseline; this is in part due to off normal incidence light making it around the sides of the LVF and illuminating the photodiode array. This is not an issue when the collimator is in place, as the collimator extends past the LVF, cutting off light not incident on the glass. A key design consideration of the spectrometer was choosing an appropriate collimator to maximize the signal while matching the resolution to that of the LVF.

The LVF is made up of different filters to control the allowed light. A step filter is used to cut off nearby peaks that can be caused by half-integer multiples of the pass-through wavelength. With very diffuse light, the step filter can lose effectiveness, allowing additional peaks to form. This may be what is being seen at the edges of the measured spectrum. It is also probable that additional light can be illuminating a portion of the photodiode array by going around the edges of the LVF. The peaks at the edges both get eliminated with the inclusion of the collimator.

The spectral resolution of the full spectrometer is impacted by each of the individual components. The theoretical resolution of the spectrometer is based on: the characteristics of the photodiode, the LVF resolution, the collimator aspect ratio and the spacing between each element. The spacing between the LVF and the photodiode array can play a significant role in the resolution of the spectrometer. If the spacing is larger, photons that exit the LVF at an angle can be detected by a photodiode element to the sides of the expected photodiode, effectively lowering the resolution of the spectrometer. To minimize this effect, the LVF was placed directly on the photodiode array.

With the LVF directly on the photodiode array, a ~1% resolution can be achieved, according to the manufacturer. Using the krypton calibration source, the resolution of the spectrometer can be measured in free space without scattering the light (chapter 4). This was determined to be approximately 13 nm using 1300 nm light, as expected. Using the model shown in figure 8A, we found a height of 400 μm with a pore size of 100 μm would produce the largest signal without degrading the resolution beyond the limits of the rest of the system. Increased collimation would not result in improved resolution, but solely a loss in signal. An aspect ratio of 4 gives an allowed angle of 14.3 degrees, as determined by equation 3.

The diffuse light data in figure 8D gives a measured FWHM resolution of 13 nm at 1300 nm, as predicted by the modeling. The spectra shown in figure 8D have a upward trend in the peak intensity with wavelength. This is primarily due to the characteristics of the light coming out of the monochromator. Data 900 nm and 1600 nm while part of the detected spectrum, are not plotted in the figure because the light from the monochromator was so dim it was difficult to distinguish from the noise.

Before each data session, a spectrum was collected with the light source off. This was used as a dark spectrum and subtracted from subsequent illuminated spectra. A recent dark spectrum subtraction will result in zero (with noise) in non-illuminated sections of the spectrum. However, in an open room the dark signal can drift with temperature. No illumination, i.e. zero intensity, was expected on some portions of the graphs, but non-zero values were manifest. This may be due to the drift in dark signal during the timeframe required to make adjustments and take data.

For human subject testing (Figure 9), a spectrum was collected on the wrist using the Flame spectrometer and our miniaturized spectrometer. The miniaturized spectrometer shows a

significant throughput improvement (100x). It is hypothesized that the improvement is due to the size of the collection area required for each technology. For the Flame, the light collection occurs at a small slit that illuminates a grating. This small area reduces the amount of light being detected, along with the internal grating and optics which all contribute additional losses in intensity, the sum of which results in long integration times (5500 ms). With the miniaturized spectrometer, the light collected is limited to the size of the pixel, with losses only due to the LVF and collimator; this allows for significantly reduced integration times (35 ms). For this test, the wavelengths were compared by aligning the peaks of the miniaturized spectrometer's spectrum with that of the Flame.

The pulsatile measurements were collected to show that the data collection is quiet and fast enough to see the pulse in a wearable situation. While the pulse collected was not very large compared to the full spectrum (600 ADC counts peak to peak vs ~51000 ADC counts background), no optimizations were done to improve the signal once placed on the participants wrist. It is believed that with more optimal placement and pressure the quality of the pulse could be significantly improved. The 1050 nm peak was chosen to illustrate the pulse, as it has the highest signal and the largest pulse. This could be used as a reference to other wavelengths to help find the pulse at wavelengths with much lower signals.

3.6 Conclusions

The results of a miniaturized SWIR (900-1650nm) spectrometer for wearable applications have been shown. With the use of a CNT collimator, this spectrometer can filter out diffuse light, making it useable for biological experiments. By tunning the collimator pore dimensions, the pass-through intensity can be maximized and the resolution limiting of the collimator can be matched to that of the other elements in the spectrometer. Thus, the

spectrometer was shown to have a spectroscopic resolution of 13 nm FWHM @ 1300 nm, which is limited by the current LVF used. The noise in the dark current at constant temperature is -28 dB. While the spectrometer currently is small and quiet, further customization of the individual components still provide some gain in size and noise performance. Physiological measurements were performed under an IRB protocols and included building it into a wearable form and pairing it with illumination sources to collect physiological data. A spectrum on the body was collected and the throughput was compared to that of a commercial spectrometer. Using LEDs, a pulse was collected on an individual. The measured signal shows the spectrometer's feasibility to begin collecting biomedical data.

Chapter 4: The Effect of Infiltration on Sidewall Reflections

4.1 Introduction

Vertically aligned CNTs grow in an intertangled forest that is mostly air by volume[39, 48]. The low density of material lowers the index of refraction making it close to that of air. Having a low index of refraction and a high coefficient of absorption give the CNTs a very low reflectance. The low density of material of these forests makes handling difficult[34]. A technique used to "strengthen" the forest is infiltration where a material can be added to the nanotubes in the forest effectually "growing" their diameter[36]. This reduces the open area of the forest and strengthens it by making the tubes larger and connected together. Infiltrating the CNTs with carbon increases the density of the material increasing reflectance off the forest[38].

Due to the absorptive properties of CNTs, they were chosen for use as a collimator as shown in chapter 2 Figure 3. In that work it was shown that with carbon infiltration, double reflections off the sidewalls of a collimator are measured. Single reflections are also expected but were not measured due to the experimental setup.

In this chapter we will show how infiltration affects the sidewall reflection of light in CNT collimators. We will show the importance of having minimal sidewall reflections in the CNT collimator as part of the miniaturized spectrometer shown in chapter 3. While increasing infiltration makes the collimators more structurally robust, allowing them to be removed from the substrate, it increases sidewall reflection. We will show that we can grow non-infiltrated collimators on transparent substrates such as Corning® Eagle glass and fused silica. These collimators have significantly reduced sidewall reflection that results in improved spectrometer

performance. While the non-infiltrated collimator is quite fragile, they could be mounted as part of a spectrometer.

4.2 Motivation

It was observed in section 2.4 that some off angle light is able to pass through the collimator by reflecting off of the sidewalls. These sidewall reflections proved to be an issue not observed in the work done in chapter 3 We hypothesize that this reflection effect was present in the work done in chapter 3, but was not observed due to the small size of the signals being detected. We expect the infiltration of the collimators to increase the index of refraction by increasing the density of the forest and while also smoothing the sidewalls both increasing the reflectivity. Infiltration improves the mechanical robustness of the collimators making handling straightforward. The infiltrated collimators were removed from the silicon samples and handled directly, but carefully using wafer tweezers. One challenge with the non-infiltrated collimators is their fragility. Without infiltration the collimators could not be removed from the substrate in a way that did not damage the collimator. This created the need for growth on a transparent substrate so the substrate could be included in the optical path.

In work with the spectrometer, we found that in some diffuse light experiments, light was detected at wavelengths that were not expected. An example of concern was that when illuminating a diffuse medium with a single LED we could detect a second peak at a location that did not correlate with the LED. Preliminary studies focused on understanding a second “peak” at moderate angles of light. In this preliminary study, collimated 1000 nm light illuminates an LVF/photodiode combination and the combination is rotated through a series of angles. These studies performed without the collimator discovered that light at angles of 25-30 degrees were able to pass through the collimator at a location corresponding to longer wavelengths in the

spectrum than expected (Figure 11). The main peak also shifts slightly with angle. It is believed that this is able to occur due to the angle, the pathlength of light becomes in integer multiple of the cavity thickness allowing it to pass. To prevent a significant amount of extra pass-through points the LVF has an additional 2 coarse band pass filters, one that is designed to block the nearest resonant wavelength and one blocking all light outside the predetermined band (190-2500 nm). These coarse bandpass filters do not shift with tilt in the same way the pass wavelength does on the wedge. We hypothesized that at high tilt angles the light is able to pass through the course band pass filter allowing for an additional peak to appear. With that hypothesis we then wanted to understand how that light was able to pass through the collimator.

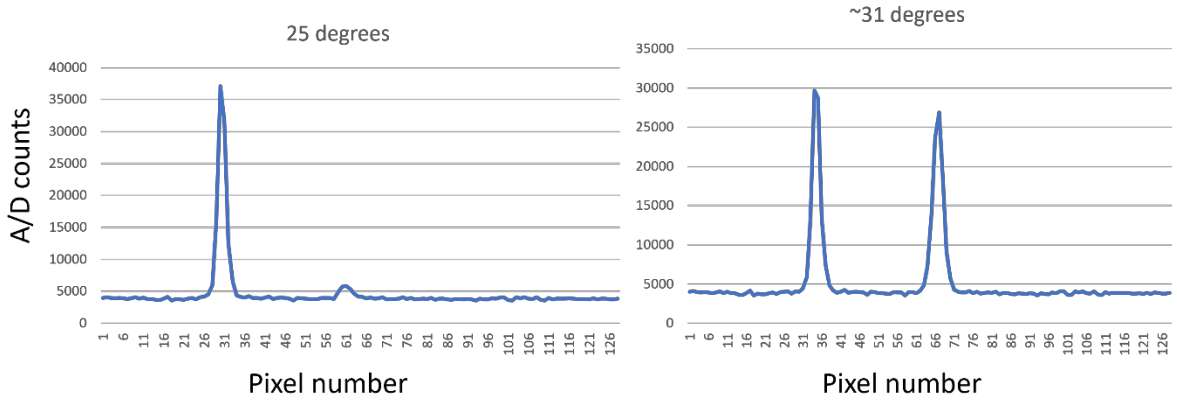

Figure 11) *A measured spectrum with angle. A photodiode/LVF pair were used to measure 1000nm light as the pair were rotated. As the angle increased a second peak appeared in the spectrum at 25 degrees (left) and grew to almost match the main peak at 31 degrees (right). Both are plotted in pixel number as the spectrometer has not been fully assembled.*

4.3 Methods

CNT growth was similar to the sample preparation and growth process described in chapter 2 with the following changes. Growths for non-infiltrated CNTs were done on

transparent substrates (both eagle glass and fused silica. The results shown were for an Eagle Glass sample. 70nm of alumina was e-beam deposited onto the substrate. The transparent substrate required the exposure time in the aligner to be doubled from 10 seconds to 20 seconds. During CNT growth the samples were not infiltrated or exposed to plasma to release them from the substrate.

Spectrometer assembly was the same as chapter 3 with the exception that collimators remained on the substrate and were mounted with the substrate on top. The edges on the substrate were adhered with gel superglue to the 3D printed spectrometer housing. Data collection was done with the Hamamatsu development board and exposure times were all set to 8.5ms. A dark collection was taken and subtracted from the spectrum collected while illuminated.

Measurements were taken by placing both spectrometers (infiltrated and non-infiltrated) at approximately the same location and 30-degree angle above a 1050nm LED (Figure 12). Due to the angular spread of the LED lens some light will be normal incidence on the spectrometer while most will not. If there were no reflections, we would expect a single peak at 1050 nm. The

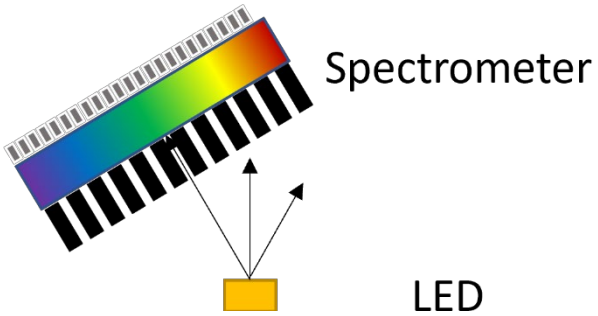

Figure 12). *Schematic of the setup used to test off normal incidence light. The LED was placed flat down on a table. The spectrometer was then tilted and rotated around the LED to where more than one peak was found, and the spectrum collected. The same location and tilt was then collected with a non-infiltrated collimator. (distances and angles are not to scale)*

spacing between the detector and LEDs were adjusted to get a primary peak at about 12000 ADC units after dark subtraction. Figure 12 is a cartoon depicting the setup (distances and angles are not to scale).

4.4 Results

A spectrum was collected by the spectrometer at a 30-degree angle when illuminated by a 1050 nm LED (Figure 13) top. Due to the lens on the LED having a wide view angle, a peak is expected at 1050 nm. This was repeated with both infiltrated and non-infiltrated collimators. It was observed that with the infiltrated collimator a second peak was detected at about 1300 nm, this peak is not present in the non-infiltrated version. Both spectrums have had the dark current subtracted from them. In Figure 13 bottom the measurement was repeated with a 1300 nm LED. The beginning of a second peak is once again observed at a longer wavelength for the infiltrated

collimator, starting at about 1600 nm. The non-infiltrated collimator does not have the second peak.

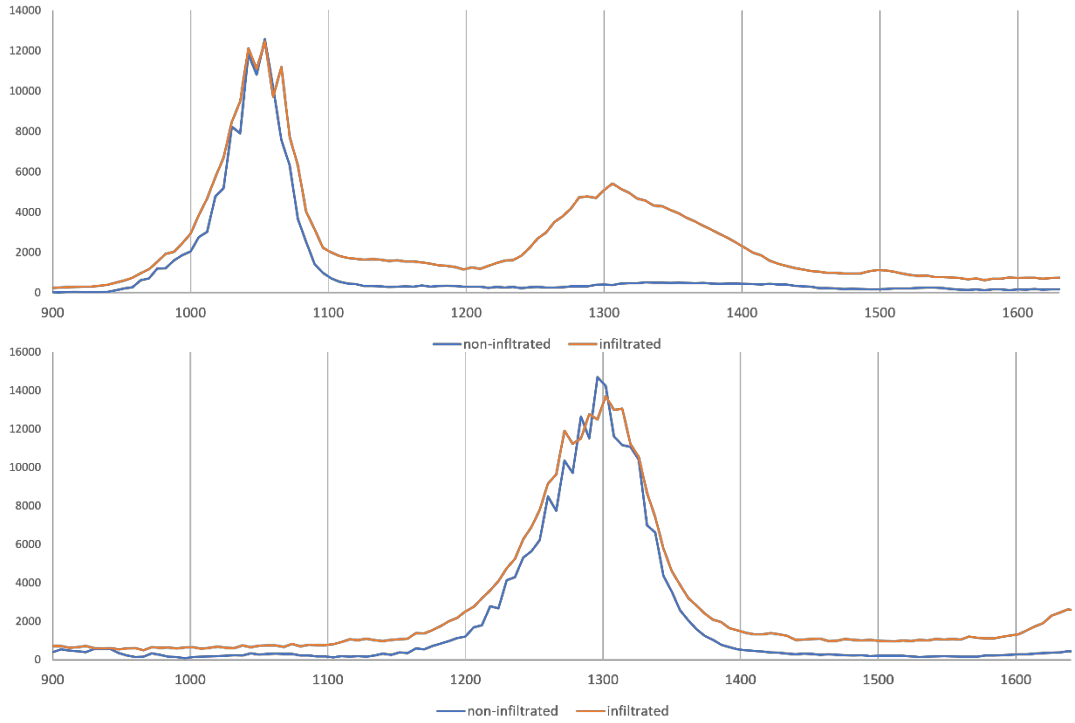

Figure 13) *Infiltrated vs non infiltrated collimators. Top) Using a 1050nm LED, light is detected at 1300nm in the infiltrated collimator, while the non-infiltrated collimator only allows the 1050 nm peak. Bottom) Using a 1300 nm LED, the infiltrated collimator dectects light at 1300 nm and 1650 nm, while the non-infiltrated collimator only detects light at 1300 nm.*

4.5 Discussion

The results from figure 13 show a difference in the allowed light for infiltrated and non-infiltrated collimators. The LED has a peak in illumination near 1050 nm, this is seen in both infiltrated and non-infiltrated collimators. The second broader peak at 1300 nm is significant for the infiltrated collimator only. This is attributed and expected due to the previously observed side wall reflections. Fabry-Perot filters have pass band harmonics from fitting extra or fewer wavelengths of light within the cavity. LVF geometries block these extra harmonics with course

band pass filtering that also shifts along the length of the LVF. Off normal incident light has a pass band that is shifted to higher wavelengths. Ie,1050 nm light will pass through the 1300 nm portion of the filter if it enters at sufficient tilt. In most cases, the addition step filter in the LVF will block this shifted pass band light. However, while the pass band and the step filters are shifting with incident light tilt, they are not shifting at the same rate. Thus, we propose that the 1300 nm signal is due to light reflecting from the sidewall of the collimator at some significant angle, passing within the shifted range of the step filters and passing through the Fabry-Perot portion of the LVF at an apparent higher wavelength position.

The LVF is rated for normal incidence light to block at least 99.5% of the signal in the out of band region(light that does not match the pass-through wavelength). This results in a small signal of about 100 ADC units being detected almost everywhere. The peaks at 1050 nm between the two tests vary in height. This may be due to experimental errors that small changes in distance between the spectrometer and LED result in significant changes in signal.

One notable feature in both graphs is the spikiness of the peak at 1050 nm. This is an expected feature of normal incident light with the collimator dimensions used. The pore size of the collimators for these experiments are 100 μm, while the pixel size of the Hamamatsu is 50 μm wide with a 50 μm gap. The collimators are not aligned with the pixels resulting in some shadowing by the collimator hedges onto every other pixel. Due to this effect the peak spikes oscillate pixel to pixel.

The non-infiltrated collimator has a distinct peak at 1050 nm and no other significant peaks. This was the expectation from a reduction in reflectance in non-infiltrated collimators. The non-infiltrated collimators were very fragile and extreme care had to be used to avoid

damage while handling or in assembly. Damage locally broadens the collimation and degrades the spectral resolution. All measurements were taken using undamaged collimators.

4.6 Conclusions

There is an observable improvement to the spectrum by the use of a non-infiltrated collimator, eliminating false peaks that pass the LVF at high tilts. With the elimination of the false second peak due to sidewall reflection, the correct spectrum of diffuse light can be collected. It was shown that the lack of infiltration can significantly reduce measured sidewall reflections. We believe that moving forward all future spectrometers will be built with non-infiltrated collimators. Some future work that was beyond the scope of this project is optimization of the infiltration or infiltration with different materials (i.e. transparent materials). This could help improve the robustness of the collimators while optimizing their absorption.

Chapter 5: Calibration of the Spectrometer

5.1 Calibration Needs

Each spectrometer is manually assembled using 3D printed parts to hold the collimator, LVF and photodiode array together. The manual assembly, and the variation in the parts used, leads to some variability from spectrometer to spectrometer. Before meaningful data can be extracted, calibration measurements need to be taken with each spectrometer. Calibration measurements include: 1. measurement of a wavelength standard, 2. measurement of the resolution 3. dark current measurement, 4. bright field measurement

Alongside bright field measurements, dark current measurements are necessary because dark current and responsivity vary from pixel to pixel due to variations in the InGaAs and the electronics used. These variations are accounted for through dark current subtraction and bright field (or flat field) correction. The dark current measurements were taken illumination source off. Traditional bright field correction is performed by illuminating all pixels with equal light and measuring the varied responses. However, this cannot easily be done once the linear variable filter (LVF) is in place. Thus, modified bright field measurements were performed by illuminating the spectrometer with a source of known broad spectrum that illuminates every wavelength region of the spectrometer.

The spectrometer studied in this work outputs the intensity data in an analog video signal where the intensity measured at each pixel is represented by a voltage with each pixel corresponding to a particular wavelength. Thus, wavelength calibration is required to determine the wavelength of light measured by each pixel. For this calibration, a krypton calibration lamp

with a known spectrum and clearly defined sharp peaks is used. Dark current measurements are taken in a lab and in a temperature-controlled chamber to get noise characteristics. Finally, a bright field spectrum from a broad tungsten halogen bulb is used to calibrate the spectrometer for measurements.

5.2 Calibration Methods

The data collection was done using the development board provided by Hamamatsu corporation and the Teensy microcontroller-based data collection system described earlier[46]. Wavelength calibration was done using a Krypton arc lamp. The spectrometer was placed 25 mm away from the lamp and a spectrum was taken with an integration time of 8.5 ms. The peaks of the measured spectrum correspond to known wavelengths[49], allowing certain pixels to be matched to the known wavelengths. A calibration vector was then built and used for a pixel-to-wavelength conversion.

The dark current was measured by taking several spectrums while the spectrometer was not illuminated. The cycle time was 10 ms, with an integration period of 8.5 ms and a data collection period of 1.5 ms. The spectra were averaged together to yield a dark current offset.

Spectrometer noise performance and temperature dependance were characterized in a temperature-controlled chamber at 25 °C. To characterize noise, dark current was measured in a temperature-controlled chamber for 20+ hours. The charge from each pixel was converted to an analog video signal and all 128 pixels were recorded every 10 ms by the microcontroller.

The temperature dependence of the spectrometer dark signal was measured. In this test the chamber temperature was varied in a controlled manner in the range of 0-40°C while

collecting data with the non-illuminated spectrometer. As with the noise measurements, data was recorded every 10 ms.

Bright field calibrations are done by illuminating the spectrometer with a broad tungsten halogen (Ocean Optics LS-1) source. To mimic the expected applications and eliminate shadowing by the collimator, the light was scattered using a diffuse reflector (Thorlabs DG10-120-P01) prior to detection (Figure 14). The spectrum was collected using the Hamamatsu development board with an integration time of 8.5 ms. The resulting spectrum is then used to make a brightfield calibration vector to correct for the pixel-to-pixel variation. First, the dark current is subtracted from the spectrum, then because the source should have a smooth continuous spectrum a 5-boxcar average is used to smooth each pixel giving us a bright field value for each pixel. The value is divided by the non-averaged pixel value to get a vector that can be multiplied by a spectrum to correct for the bright field.

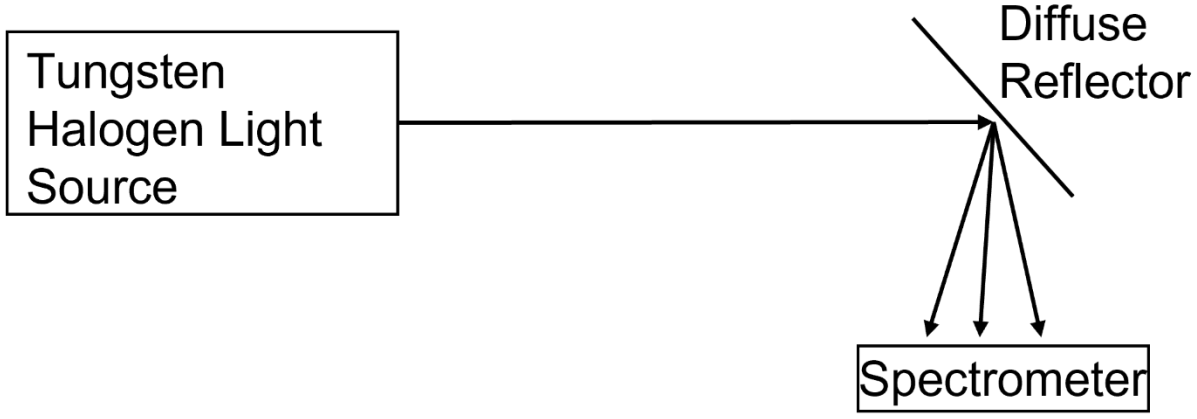

Figure 14). *Setup for bright field testing. Using a tungsten halogen bulb and a diffuse reflector, a scattered broad spectrum illuminates the spectrometer. The resulting data can be used to calculate the bright field correction for the spectrometer.*

The resolution of the spectrometer was calculated using a spectrally narrow source at various wavelengths. In the main text this was done with a monochromator; here it was also done using the krypton arc lamp. The resolution of the spectrometer is determined by the full width half max (FWHM) of the sharpest peak (1363 nm).

Using the diffuse reflector to scatter light from five LEDs (Marktech 1050 nm, 1300 nm, 1550 nm, 2x 1650 nm), the effect of dark current and bright field corrections are shown. The raw spectrum from the LEDs is collected using the Hamamatsu development board. The dark current is then subtracted from the spectrum and the bright field correction applied.

5.3 Calibration Results

A Krypton arc lamp gives off a known spectrum with narrow peaks at known wavelengths (such as 975 nm, 1363 nm, 1442 nm, 1523 nm). A spectrum collected from our spectrometer when illuminated by a Krypton arc lamp is shown in figure 15. The collected spectrum is overlaid with the peaks using a peak-finder application and their relative sizes. This gives multiple calibration points from which the rest of the wavelengths are extrapolated assuming a linear fit in between data points. The pixel-to-pixel spacing is approximately 6 nm.

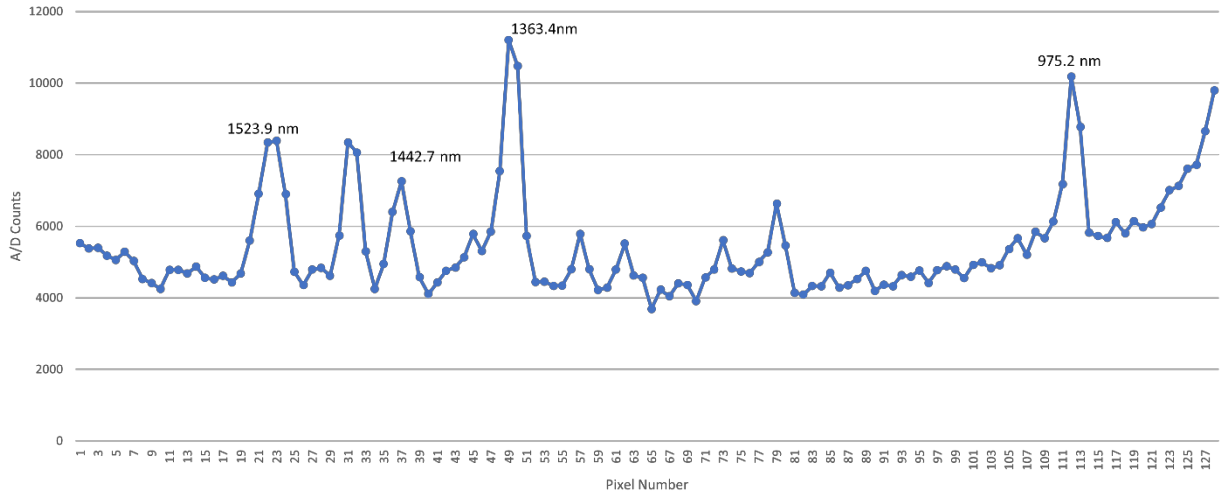

Figure 15). *The spectrum of light collected from a krypton arc lamp. Light is collected from a krypton arc lamp and a spectrum measured. The peaks in the spectrum match with known peaks from the krypton source*

With a means of calibrating each spectrometer, we can look at the spectrometer-to-spectrometer variations between builds. With the pixel pitch of the photodiode array being 50 µm, a slight shift during assembly will result in a shift in wavelength. A few devices were calibrated and compared to each other by plotting them on the same scale as shown in figure 16. The location of the peaks varies by up to two pixels. The height and width of the peaks also vary. Note that the LVF was oriented in the opposite direction as figure 15. All the devices were measured under the same conditions, but the spectrum of each device is unique and need to be normalized for use.

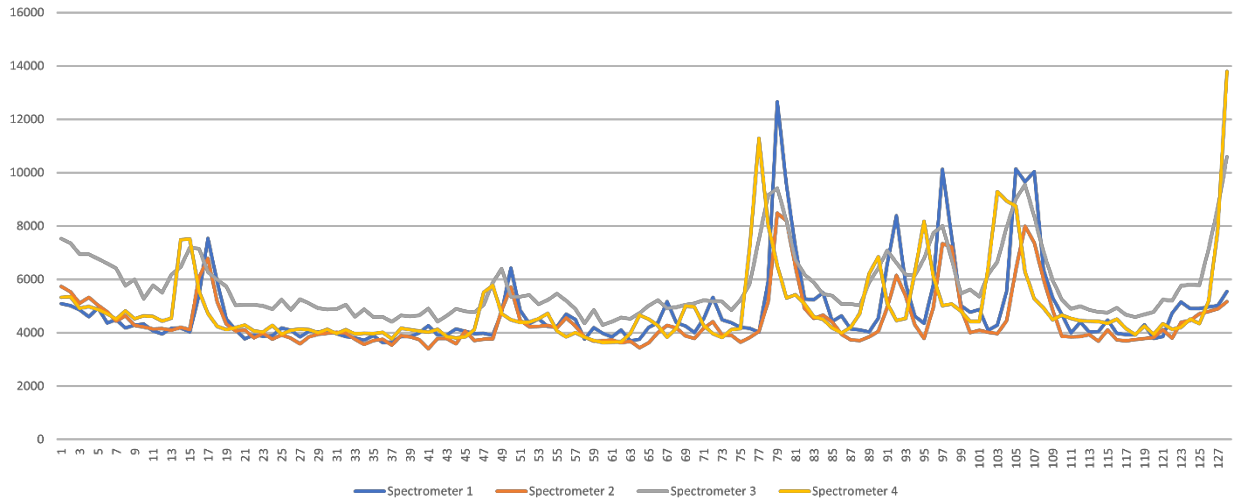

Figure 17). *Four different spectrometers measure the same spectrum from a krypton arc lamp. The krypton spectrum can be used as a way to see the differences in the spectrometers from build to build.*

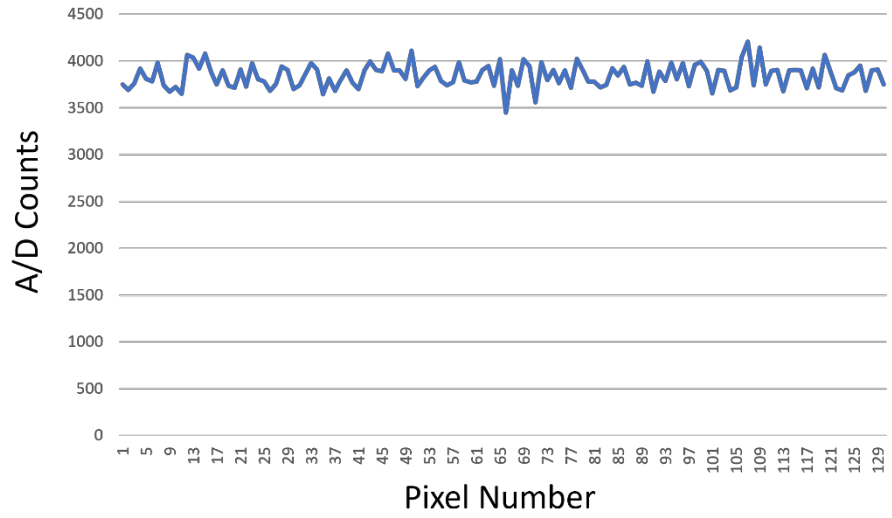

Figure 16). *A dark current measurement. By taking measurements with the spectrometer with the light source turned off a signal that is due to the dark current in the electronics. This spectrum can be subtracted from any spectra collected by the spectrometer to improve the signal*

Dark current measurements allowed for the development of a dark current correction vector. The dark spectrum was collected every 10 ms for three second total. These spectra were then averaged together to produce figure 17. Figure 17 shows the different dark current from

pixel to pixel. This spectrum is subtracted from an illuminated spectrum to perform the dark current correction.

For a time period of 20+ hours the spectrometer collected data at constant temperature in 10 ms intervals. The spectrometer was blocked from light to study the noise in the dark current. The mean (over multiple measurements) dark current (~1200 ADC counts) was subtracted from each data point (figure 18 top). Grouping the results into 1000 equal size bins the standard deviation was calculated and plotted in S5 bottom. The standard deviation was calculated to be 6 ADC counts, which coverts to a noise level of -28 dB.

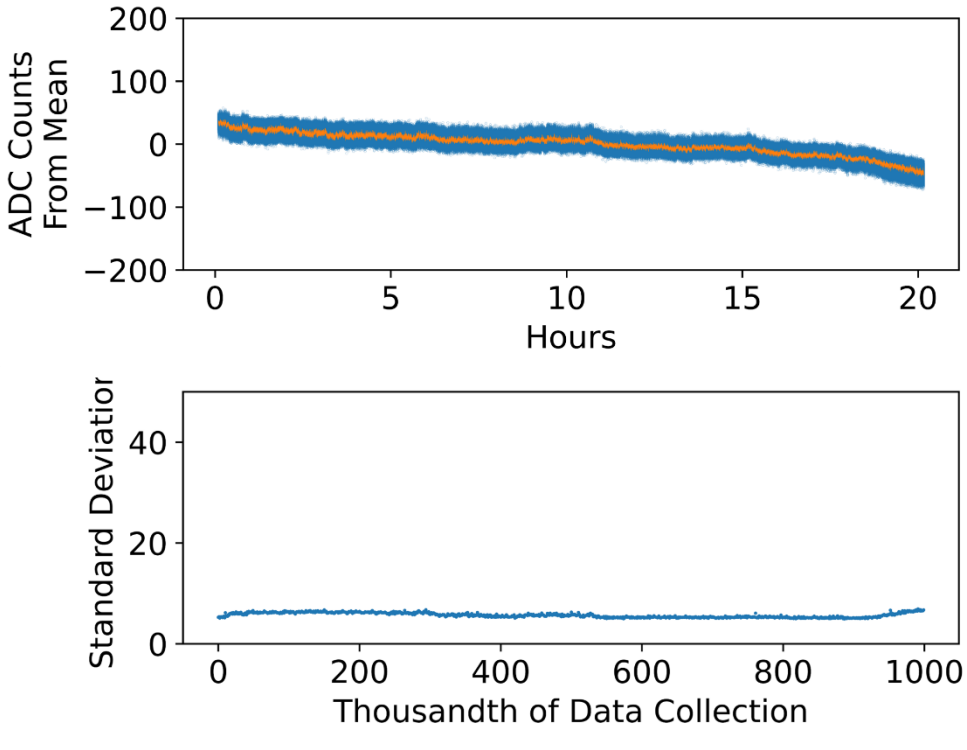

Figure 18). *Dark current measurements at a constant temperature. Top) Showing one pixel measured in time, the dark current fluctuations are plotted with the mean dark current removed. Bottom) The data from the top graph is grouped into 1000 bins of equal size and the standard deviation calculated and plotted. The mean standard deviation was found to be 6 ADC counts, which equates a noise of -28 dB.*

A shorter run of 1.75 hours with varying temperatures measured the change in the dark current with temperature (Figure 19 bottom). The temperature-controlled chamber was programmed with the temperature profile in figure 19 top. While ranging the temperatures from 0-40 °C, the dark current of a single pixel varied from 600 ADC to 1600 ADC counts. As temperature increases the ADC counts also increase. While the base ADC counts do not directly

correlate with a given temperature, large changes in temperature yield more drastic changes in ADC counts.

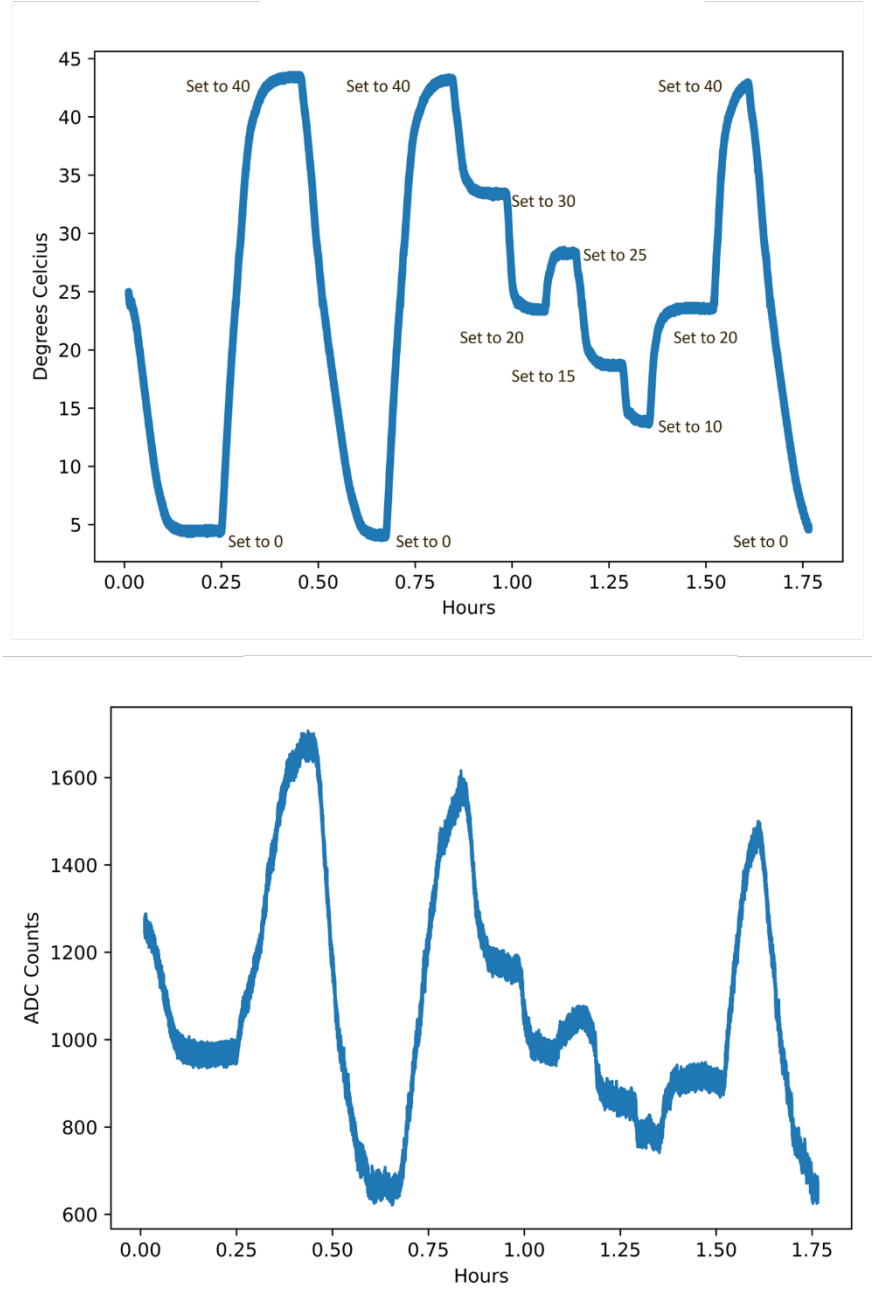

Figure 19). *Dark current measurements with changing temperature. Top) The temperature profile input into the temperature controlled chamber. Bottom) The dark current measurements for 1 pixel with changing temperature.*

Bright field calibration is developed from a measurement made by illuminating the spectrometer with a tungsten halogen light source (Figure 20). In the raw spectrum, there are some noticeable pixel-to-pixel fluctuations. After dark current subtraction, a pixel-by-pixel vector is developed to normalize the spectrum to match the light source. This is then applied to future measurements.

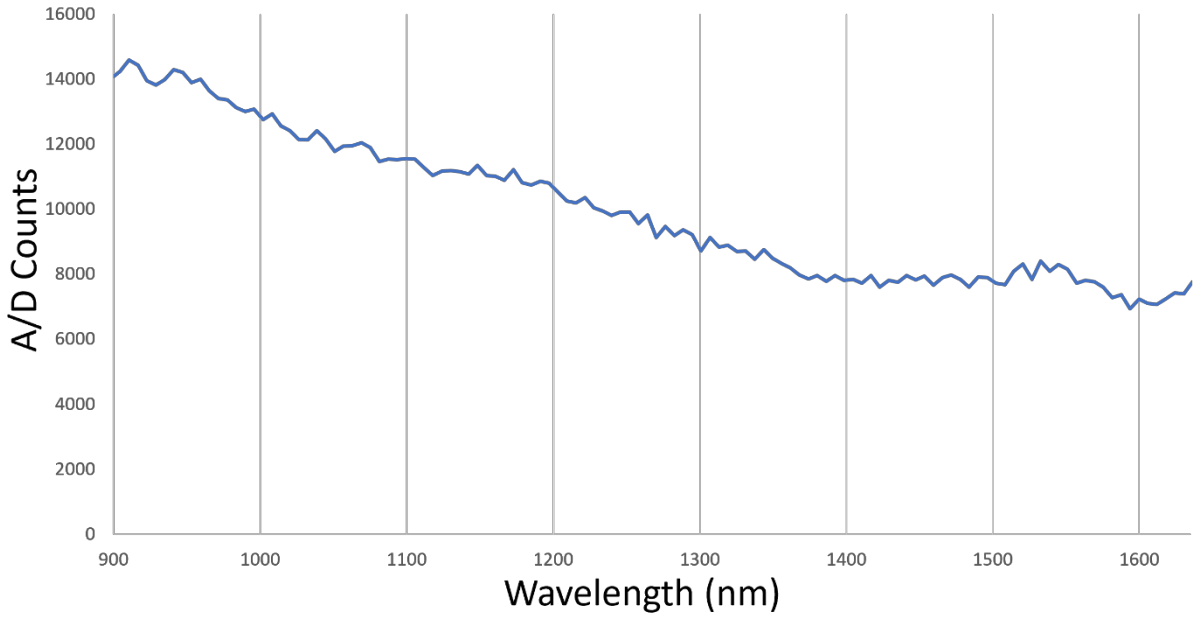

Figure 20). *The spectrum collected from a tungsten halogen source. The bright field vector is calculated using the spectrum and averaging the nearest pixels in a 5-boxcar average.*

Using five LEDs the spectrometer is illuminated off a diffuse reflector to collect a spectrum (Figure 21 top). The spectrum in figure 21 has artifacts of both the dark current and the variations in pixel responsivity. Most notable is the dip in the spectrum just before 1500 nm. Applying the dark field subtraction and bright field calibration to the original spectrum, we get a corrected spectrum (Fig 21 bottom). This corrected spectrum is smoother than the raw spectrum collected. Looking just before 1500 nm, the raw waveform has a dip in intensity, after calibration

that dip is no longer there. The “roughness” of the signal around 1200 nm is also reduced after calibration.

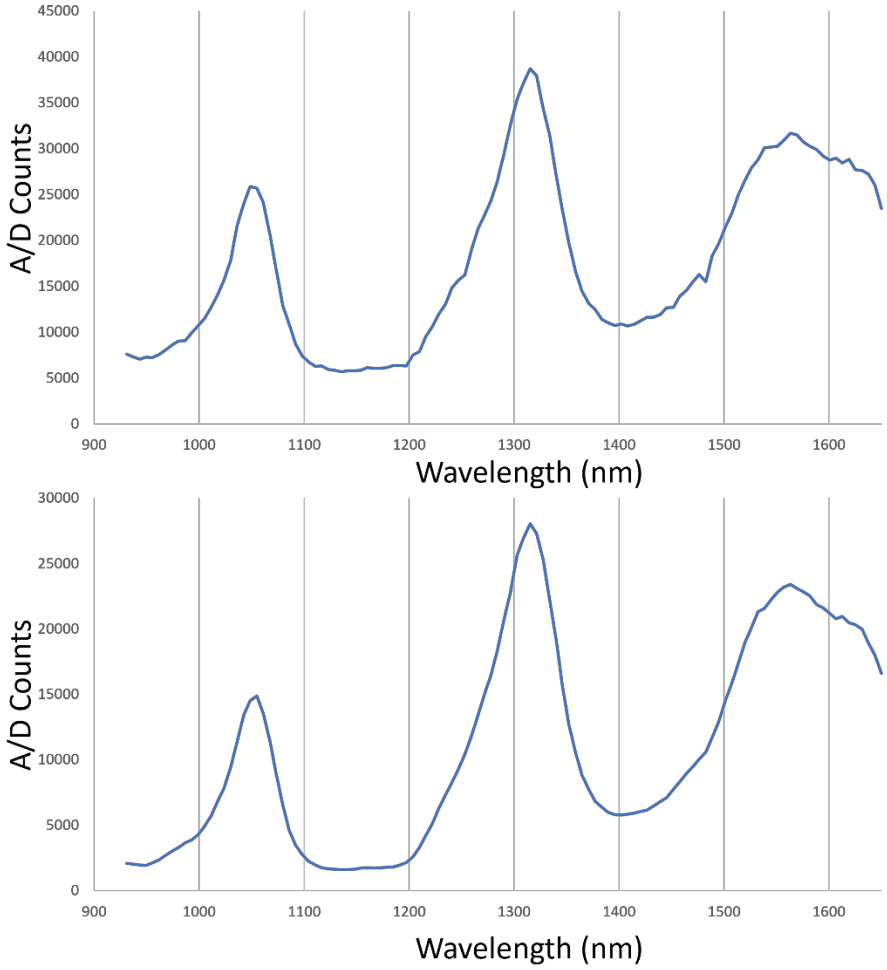

Figure 21). *Bright field calibrations. Top) The raw spectrum collected from the LEDs off a diffuse reflector. Bottom) The spectrum from the LEDs off a diffuse reflector after dark current subtraction and bright field correction.*

5.4 Discussion

A krypton arc lamp provides a reliable metric to test each spectrometer build, to both calibrate each device by wavelength and determine the spectrometer-to-spectrometer variations in wavelength and resolution. The spectra from figure 15 to 16 are flipped, due to the orientation of the LVF in reference to the photodiode array. The orientation of the LVF to the photodiode

array is arbitrary during assembly. If careful care is not taken, the spectrometers can output spectral features at very different pixel numbers. In figure 16 there appears to be a 2-pixel shift from spectrometer 1 to 4; this would result in about a 12 nm shift between spectrometers.

After wavelength calibration, the resolution of the spectrometer can be calculated by looking at a sharp peak like the one at 1363 nm. By taking the full width half max of the peak, we determine the resolution of the spectrometer at that wavelength. A typical spectrometer has a resolution of 13-14 nm at the 1363nm peak. Spectrometer 3 is unique, as the majority of the spectrum is higher than the other 3 spectrometers and its peaks are broader. This indicates that the collimator used to build this spectrometer was shorter than the rest, allowing more light through while broadening each peak. This is also represented in the much lower resolution of this device (~20 nm). This method of testing spectrometers allows for an analysis of the unit as a whole, which could help with quality control of the devices.

The dark current measurements are straightforward; due to laboratory light outputting little to no light in the 900-1700 nm range, a dark current measurement could be made in an open indoor room while the spectrometer illumination sources are off. The InGaAs photodiode is nonresponsive to light outside the 900-1700 nm range. Several dark scans were collected and averaged to minimize noise in the dark measurement.

The integration time for the noise performance was chosen to be 8.5 ms as this is the expected application-based integration time. All the measurements thus far were collected using the development board provided by Hamamatsu. Hamamatsu also provided the collection software, but that software was designed to take single spectra or continuous spectra for a minute or two. This was not suitable for a long multi-hour run. We solved this by building a collection

system using a Teensy 3.5 microcontroller. The collection system was designed to have lower noise than the expected noise from the Hamamatsu detector.

The standard deviation of the collection system noise was -28dB. Calculations based on datasheets of the Hamamatsu detector found the primary source of the noise to be the write noise of the device. While it would be preferential to be shot noise limited, the write noise was related to the read out integrated circuit (ROIC) on the Hamamatsu diode and was not alterable for this work. Further optimizations could be possible but were not the focus of this work as the noise is small compared to the full scale.

InGaAs detectors have sensitivity to changes in ambient temperature. It was important to verify the dependance for future temperature-based calibrations. Using the temperature-controlled chamber, temperatures could be reliably varied. Figure 19 gives a clear temperature dependance with the base A/D counts rising with increased temperature. The counts had a range of about 1000 A/D counts from 0-40°C. Even small changes in temperature had large changes in the dark current offset when compared to the noise. The spectrometer seemed to become less sensitive to high temperature swings as the experiment continued. This can be seen as the peaks get lower with each 40 °C measurement. This may be due to shorter time at each point, which may have been too short for the temperature to stabilize.

Bright field measurements were collected using a tungsten halogen source as it was a smooth broad source. The assumption was made that the illumination intensity for a nearby pixel was expected to be the same, justifying the use of the boxcar average. While not an ideal bright field, it is close and can still improve data quality. In a production setting, an bright field would be collected before spectrometer assembly; this would enable a flat field measurement to be taken and averaged. This was not practical as several spectrometers have been built and there is

not a straightforward way to identify the individual photodiodes when not a part of a spectrometer. This would not be an issue in a production environment.

Using the dark current and bright field calibrations, the quality of the measured spectrum can be improved. The spectrum collected from LEDs can be smoothed out. LEDs were chosen as a baseline for the spectrum going into the body for human subjects testing. The calibration also gives more meaning to the individual intensity values as the gain from pixel to pixel is accounted for. All of the calibrations shown here are important to have done for each spectrometer to ensure quality control and quality data.

5.5 Conclusions

A method of calibrating each spectrometer built, while establishing a means to look at the quality control of a group of spectrometers is shown. While none of the techniques used here were novel in their approaches, they were important steps in calibrating and validating the spectrometer shown in this work.

We have shown that wavelength calibration is important as a quality control for each spectrometer because of the variation in the alignment of the linear variable filter with the photodiode array and height of the collimator. A small shift in the filter location can offset a wavelength peak by 1 to 2 pixels, which corresponds to 6-12 nm. The quality control can also act as a check for validating that the collimator heights between units are within a given tolerance, as shorter collimators will have larger base ADC counts and broader peaks.

We have shown the importance of dark current and bright field calibrations as well as quantifying the dark current noise. The dark current noise was small at -28dB but does limit the signal to noise if used in a highly sensitive measurement. Temperature fluctuations will need

further study to quantify the expected change with temperature in a wearable application. Using the spectrometer in a well understood test we were able to develop calibration vectors to improve the quality of measured signals. We are able to reduce the “jaggedy” nature of the raw waveform to more accurately represent the collected spectrum. The calibration gives more meaning to the data by translating pixels to wavelengths and by decreasing inaccuracies related to variation in intensity. It is important moving forward for these calibrations to be performed for each spectrometer.

Chapter 6: Conclusions and Suggestions for Future Work

6.1 Collimators

In this work we show the development and characterization of a miniaturized collimator and spectrometer. Using CNT microfabrication, we showed that high aspect ratio CNTs can be used as an effective parallel hole collimator. The tolerance of allowed angles of light are controlled by the height and pore size of the collimator and can be predicted mathematically using a geometric model. While these collimators effectively cut off allowed light at the predicted cut off angle, there was light measured outside the expected range. This light was hypothesized to be due to reflections off the sidewalls of the collimator.

Sidewall reflections were shown to significantly hinder the quality of data collected from the spectrometer. To resolve this issue, growths without infiltration on transparent substrates were studied. While the transparent substrates did not change to CNT preparation process, they allowed for the CNT's to be left on the substrate when used with a spectrometer. As they did not need removing, infiltration of the CNTs was not necessary for handling and removal from the substrate. Testing on non-infiltrated CNTs did not exhibit the additional peaks indicating sidewall reflections that the infiltrated CNTs did.

6.2 Spectrometer

Using the CNT collimator a miniaturized linear variable filter-based spectrometer was developed. This spectrometer was modeled and characterized. Modeling showed the expected performance of the LVF based on collimator height. Spectral characterization showed the spectrometer had a spectral resolution of 13nm at 1300nm, matching the specifications of 1% of the LVF used. Noise characterization showed that our own data collection system had low noise

with a dark current noise of -28dB. The miniaturized spectrometer was compared to a commercial spectrometer with similar spectral resolution. The commercial spectrometer used a traditional diffraction grating for wavelength separation. When placed on the body with a broad-spectrum tungsten source the miniaturized spectrometer was over 100x more sensitive.

The miniaturized spectrometer is designed to output data based on pixel number not wavelength. We used a krypton arc lamp as a calibration source to convert pixel numbers to wavelength. We also showed the importance of using the calibration spectrum as a quality control to normalize spectrometers as there could be a shift by multiple pixels for a known wavelength during construction. We also discussed the value of the spectrum collected as a verification that the collimator meets the expected collimation for use.

As an initial study to validate the spectrometer in vivo spectrums were collected. Using a human subject, the spectrometer in junction with LEDs was placed on the wrist. Spectrums were collected for a period of a few minutes, and a single pixel was plotted showing a pulsatile waveform. This measurement shows the spectrometer being used to collect a relevant biological signal, making it useable for wearable physiological measurements.

6.3 Future Work

While beyond the scope of the work shown here there are further optimizations that should be studied on both the collimator and the spectrometer. As a solution to the sidewall reflections, non- infiltrated collimators were studied and shown to be effective. The primary challenge with non-infiltrated CNTs is their fragility. Alternative methods to making the collimator can be explored. This may include infiltration with transparent materials on top of the non-infiltrated CNTs, as well as possible partial infiltrations. These studies could help the collimators become blacker while improving their handleability.

With the spectrometer, future work could include further miniaturization and application-based testing. Currently the spectrometer is made of 3 separate components put together, this includes the photodiode array, linear variable filter and the collimator. The linear variable filter is on a 1.5mm thick piece of glass. If this glass thickness is reduced an equivalent reduction in the thickness of the spectrometer is straightforward. It would be possible to deposit the linear variable filter directly onto the photodiode array and remove the glass entirely. The photodiode array is packaged in its own housing and if a bare die was used the spectrometer could possibly be miniaturized further.

The spectrometer was discussed in conjunction with its possible use as a health monitoring device. The efficacy and feasibility of this claim needs to be further studied. Data collection on human subjects with reference data of physiological concentrations will be needed. The human subjects studies would enable algorithms to be developed to identify correlations between the spectroscopic signatures and physiological changes in the body. Upon the development of the algorithms, it would be possible to use this spectrometer into a continuously wearable, health monitoring device.

IRB: All human subjects testing was performed through an approved IRB process at BYU.

Bibliography

1. Lupton, D., The digitally engaged patient: Self-monitoring and self-care in the digital health era. *Social Theory & Health* **2013,** *11* (3), 256-270.
2. Fullerton, B.; Jeitler, K.; Seitz, M.; Horvath, K.; Berghold, A.; Siebenhofer, A., Intensive glucose control versus conventional glucose control for type 1 diabetes mellitus. *Cochrane Database of Systematic Reviews* **2014,** (2).
3. Rodriguez-Gutierrez, R.; Gonzalez-Gonzalez, J. G.; Zuñiga-Hernandez, J. A.; McCoy, R. G., Benefits and harms of intensive glycemic control in patients with type 2 diabetes. *bmj* **2019,** *367*.
4. Villena Gonzales, W.; Mobashsher, A. T.; Abbosh, A., The progress of glucose monitoring—A review of invasive to minimally and non-invasive techniques, devices and sensors. *Sensors* **2019,** *19* (4), 800.
5. Shang, T.; Zhang, J. Y.; Thomas, A.; Arnold, M. A.; Vetter, B. N.; Heinemann, L.; Klonoff, D. C., Products for monitoring glucose levels in the human body with noninvasive optical, noninvasive fluid sampling, or minimally invasive technologies. *Journal of Diabetes Science and Technology* **2022,** *16* (1), 168-214.
6. Moström, P.; Ahlén, E.; Imberg, H.; Hansson, P.-O.; Lind, M., Adherence of self-monitoring of blood glucose in persons with type 1 diabetes in Sweden. *BMJ Open Diabetes Research and Care* **2017,** *5* (1), e000342.
7. Serup, J.; Jemec, G. B.; Grove, G. L., *Handbook of non-invasive methods and the skin*. CRC press: 2006.
8. Pantelopoulos, A.; Bourbakis, N. G., A survey on wearable sensor-based systems for health monitoring and prognosis. *IEEE Transactions on Systems, Man, and Cybernetics, Part C (Applications and Reviews)* **2009,** *40* (1), 1-12.
9. Cote, G. L., Noninvasive and minimally-invasive optical monitoring technologies. *The Journal of nutrition* **2001,** *131* (5), 1596S-1604S.
10. Amerov, A. K.; Chen, J.; Small, G. W.; Arnold, M. A., Scattering and absorption effects in the determination of glucose in whole blood by near-infrared spectroscopy. *Analytical chemistry* **2005,** *77* (14), 4587-4594.
11. Yusoff, I.; Yahya, R.; Omar, W.; Ku, L. In *Non invasive cholesterol meter using Near Infrared sensor*, 2015 Innovation & Commercialization of Medical Electronic Technology Conference (ICMET), IEEE: 2015; pp 100-104.
12. Amerov, A. K.; Chen, J.; Small, G. W.; Arnold, M. A. In *The influence of glucose upon the transport of light through the whole blood*, Complex Dynamics, Fluctuations, Chaos, and Fractals in Biomedical Photonics, International Society for Optics and Photonics: 2004; pp 101-111.
13. Cunningham, D. D.; Stenken, J. A., *In vivo glucose sensing*. John Wiley & Sons: 2009; Vol. 174.
14. Amerov, A. K.; Chen, J.; Arnold, M. A., Molar absorptivities of glucose and other biological molecules in aqueous solutions over the first overtone and combination regions of the near-infrared spectrum. *Applied Spectroscopy* **2004,** *58* (10), 1195-1204.
15. Hollas, J. M., *Modern spectroscopy*. John Wiley & Sons: 2004.
16. Yeh, T. S.; Tseng, S. S., A low cost LED based spectrometer. *Journal of the Chinese Chemical Society* **2006,** *53* (5), 1067-1072.
17. Yang, Z.; Albrow-Owen, T.; Cai, W.; Hasan, T., Miniaturization of optical spectrometers. *Science* **2021,** *371* (6528), eabe0722.
18. Kneubühl, F., Diffraction grating spectroscopy. *Applied optics* **1969,** *8* (3), 505-519.
19. Dami, M.; De Vidi, R.; Aroldi, G.; Belli, F.; Chicarella, L.; Piegari, A.; Sytchkova, A.; Bulir, J.; Lemarquis, F.; Lequime, M. In *Ultra compact spectrometer using linear variable filters*, International

Conference on Space Optics—ICSO 2010, International Society for Optics and Photonics: 2018; p 1056559.
20. Ekkers, J.; Flygare, W., Pulsed microwave Fourier transform spectrometer. *Review of Scientific Instruments* **1976,** *47* (4), 448-454.
21. Saptari, V.; Youcef-Toumi, K., Design of a mechanical-tunable filter spectrometer for noninvasive glucose measurement. *Applied optics* **2004,** *43* (13), 2680-2688.
22. Bacon, C. P.; Mattley, Y.; DeFrece, R., Miniature spectroscopic instrumentation: applications to biology and chemistry. *Review of Scientific instruments* **2004,** *75* (1), 1-16.
23. Crocombe, R. A., Portable spectroscopy. *Applied Spectroscopy* **2018,** *72* (12), 1701-1751.
24. Bacon, C. P.; Garcia-Rubio, L. H. In *Multiangle-multiwavelength UV/visible spectroscopy for the characterization of the joint property distribution of whole blood and its components*, Optical Biopsy II, SPIE: 1998; pp 110-118.
25. O'Brien, N. A.; Hulse, C. A.; Friedrich, D. M.; Van Milligen, F. J.; von Gunten, M. K.; Pfeifer, F.; Siesler, H. W. In *Miniature near-infrared (NIR) spectrometer engine for handheld applications*, Next-generation spectroscopic technologies V, International Society for Optics and Photonics: 2012; p 837404.
26. Wiesent, B.; Dorigo, D.; Koch, A., 3.3-A miniaturized MID-IR-Spectrometer based on a linear variable filter and pyroelectric line array–Monitoring oil condition. *Proceedings IRS² 2013* **2013**, 59-64.
27. Wiesent, B. R.; Dorigo, D. G.; Koch, A. W. In *Limits of IR-spectrometers based on linear variable filters and detector arrays*, Instrumentation, Metrology, and Standards for Nanomanufacturing IV, International Society for Optics and Photonics: 2010; p 77670L.
28. Zhang, L.; Anthon, E. W.; Harrison, J. C.; Hannan, P. G.; Van Milligen, F. J.; McEldowney, S. C.; Zarrabian, S. In *Miniature spectrometer based on linear variable interference filters*, Air Monitoring and Detection of Chemical and Biological Agents II, SPIE: 1999; pp 42-50.
29. Westover, T.; Olsen, S.; Westhoff, Z.; Morrill, N.; Davis, R.; Vanfleet, R., Visible and short-wavelength infrared light collimation through carbon nanotube, parallel-hole collimators. *Optics Express* **2022,** *30* (13), 22679-22686.
30. Chapman, G. H.; Tank, M. S.; Chu, G.; Trinh, M. In *Optical imaging of objects within highly scattering media using silicon-micromachined collimating arrays*, Optical Fibers and Sensors for Medical Applications II, International Society for Optics and Photonics: 2002; pp 187-198.
31. Chapman, G. H.; Trinh, M.; Pfeiffer, N.; Chu, G.; Lee, D., Angular domain imaging of objects within highly scattering media using silicon micromachined collimating arrays. *IEEE Journal of selected topics in quantum electronics* **2003,** *9* (2), 257-266.
32. Tank, M. S.; Chapman, G. H., Micromachined silicon collimating detector array to view objects in a highly scattering medium. *CAN J ELECTR COMPUT ENG* **2000,** *25* (1), 13-18.
33. Hayamizu, Y.; Yamada, T.; Mizuno, K.; Davis, R. C.; Futaba, D. N.; Yumura, M.; Hata, K., Integrated three-dimensional microelectromechanical devices from processable carbon nanotube wafers. *Nature nanotechnology* **2008,** *3* (5), 289-294.
34. Hutchison, D. N.; Morrill, N. B.; Aten, Q.; Turner, B. W.; Jensen, B. D.; Howell, L. L.; Vanfleet, R. R.; Davis, R. C., Carbon Nanotubes as a Framework for High-Aspect-Ratio MEMS Fabrication. *Journal of Microelectromechanical Systems* **2010,** *19* (1), 75-82.
35. Chen, G.; Davis, R. C.; Futaba, D. N.; Sakurai, S.; Kobashi, K.; Yumura, M.; Hata, K., A sweet spot for highly efficient growth of vertically aligned single-walled carbon nanotube forests enabling their unique structures and properties. *Nanoscale* **2016,** *8* (1), 162-171.
36. Fazio, W. C.; Lund, J. M.; Wood, T. S.; Jensen, B. D.; Davis, R. C.; Vanfleet, R. R. In *Material Properties of Carbon-Infiltrated Carbon Nanotube-Templated Structures for Microfabrication of Compliant Mechanisms*, 2011; ASMEDC.

37. Hanna, B. H.; Fazio, W. C.; Tanner, J. D.; Lund, J. M.; Wood, T. S.; Davis, R. C.; Vanfleet, R. R.; Jensen, B. D., Mechanical Property Measurement of Carbon Infiltrated Carbon Nanotube Structures for Compliant Micromechanisms. *Journal of Microelectromechanical Systems* **2014,** *23* (6), 1330-1339.
38. Laughlin, K.; Vanfleet, R. R.; Davis, R. C., Mechanically Robust Vertically Aligned Carbon Nanotube Composites for Applications in Ultralow Reflectance Optical Elements. *ACS Applied Nano Materials* **2022**.
39. de Los Arcos, T.; Oelhafen, P.; Mathys, D., Optical characterization of alignment and effective refractive index in carbon nanotube films. *Nanotechnology* **2007,** *18* (26), 265706.
40. Yang, Z.-P.; Ci, L.; Bur, J. A.; Lin, S.-Y.; Ajayan, P. M., Experimental observation of an extremely dark material made by a low-density nanotube array. *Nano letters* **2008,** *8* (2), 446-451.
41. Lehman, J.; Yung, C.; Tomlin, N.; Conklin, D.; Stephens, M., Carbon nanotube-based black coatings. *Applied physics reviews* **2018,** *5* (1), 011103.
42. Cui, K.; Wardle, B. L., Breakdown of native oxide enables multifunctional, free-form carbon nanotube–metal hierarchical architectures. *ACS applied materials & interfaces* **2019,** *11* (38), 35212-35220.
43. Chen, G.; Dodson, B.; Hedges, D. M.; Steffensen, S. C.; Harb, J. N.; Puleo, C.; Galligan, C.; Ashe, J.; Vanfleet, R. R.; Davis, R. C., Fabrication of high aspect ratio millimeter-tall free-standing carbon nanotube-based microelectrode arrays. *ACS Biomaterials Science & Engineering* **2018,** *4* (5), 1900-1907.
44. Sypherd, S. D., Effects of Infiltration Temperature, Time, and Gas Flow Rate on Material Properties of Carbon Infiltration Carbon Nanotubes. **2019**.
45. Emadi, A.; Wu, H.; de Graaf, G.; Wolffenbuttel, R., Design and implementation of a sub-nm resolution microspectrometer based on a Linear-Variable Optical Filter. *Optics Express* **2012,** *20* (1), 489-507.
46. Westhoff, Z. A Microcontroller-Integrated Miniature Infrared Spectrometer for Noninvasive Sensing of Physiological Signals. Brigham Young University, 2021.
47. Ware, J. P. a. M., *Physics of Light and Optics*. available at optics.byu.edu: 2015 edition.
48. Shi, H.; Ok, J. G.; Won Baac, H.; Jay Guo, L., Low density carbon nanotube forest as an index-matched and near perfect absorption coating. *Applied Physics Letters* **2011,** *99* (21), 211103.
49. Kenda, A.; Kraft, M.; Tortschanoff, A.; Scherf, W.; Sandner, T.; Schenk, H.; Luettjohann, S.; Simon, A. In *Development, characterization and application of compact spectrometers based on MEMS with in-plane capacitive drives*, Next-Generation Spectroscopic Technologies VII, SPIE: 2014; p 910102.

Appendix

S.O.P. for Thermal Evaporation

SOP of Jim

Note: The system should always be left on standby when not in use. This means that the chamber is under vacuum.

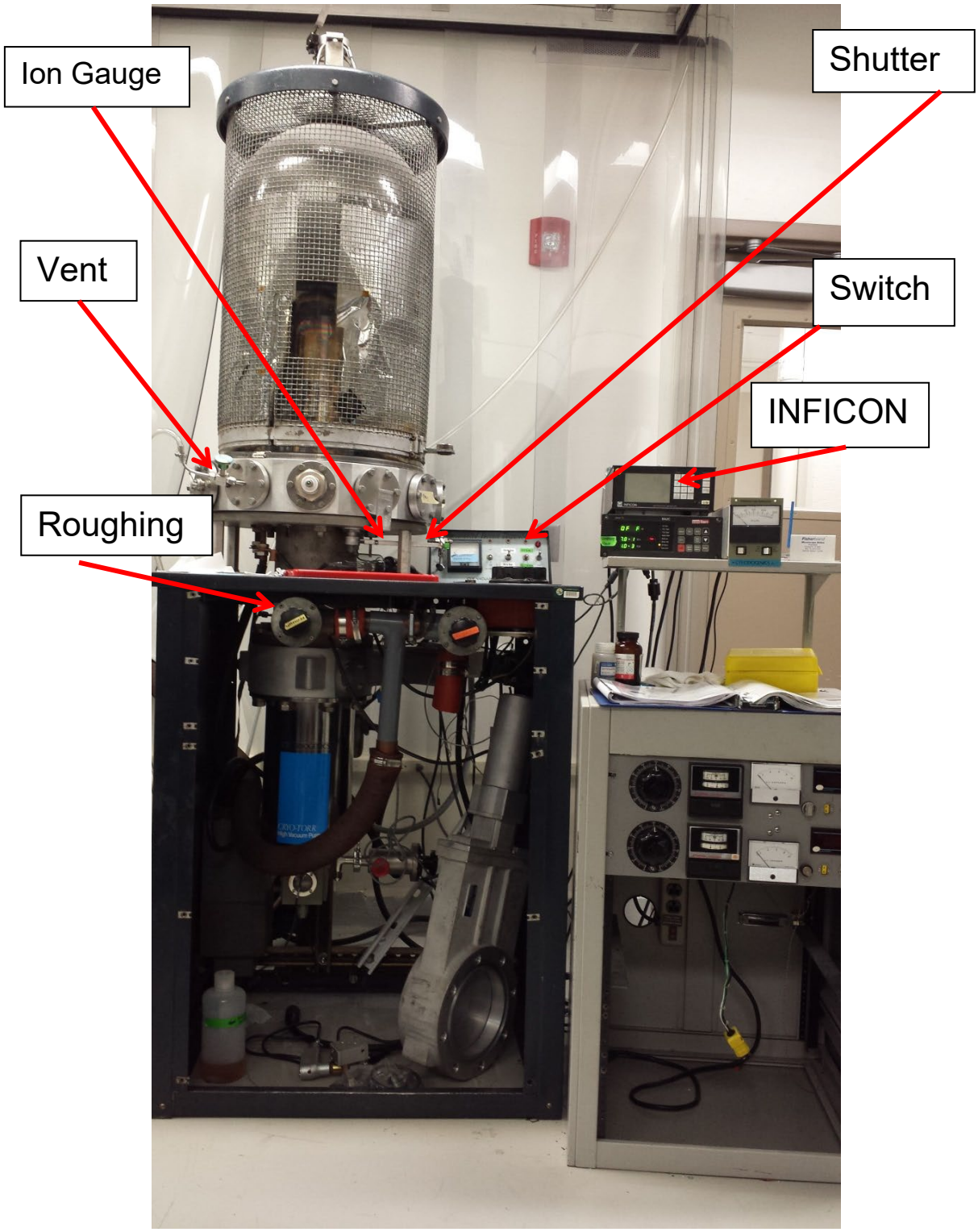

Figure 22) *Image of JIM with labels of the important pieces of equipment*

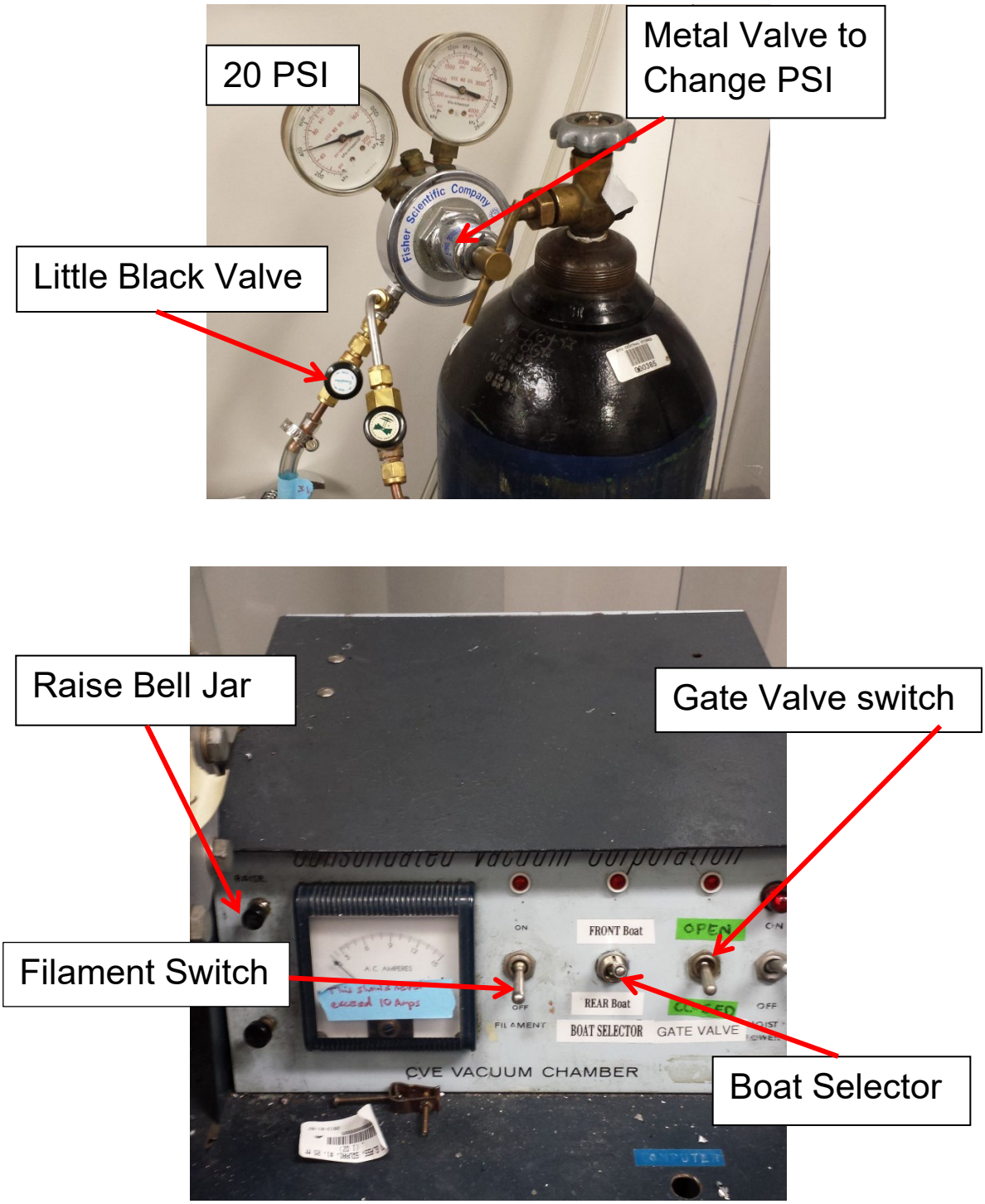

Figure 23) *Images of the nitrogen gas cylinder and control panel for JIM*

1. **Vent the chamber**
   1.1. Double check to make sure that the chamber is ready to be vented.

1.1.1. The ION GAUGE should be OFF (the bulb is NOT lit). If the bulb is ON, turn it off with the EMIS button.
1.1.2. Make sure the GATE VALVE is CLOSED.
1.2. Open the Nitrogen tank in the corner; record the pressure on the log sheet. Then open the back little black valve on the regulator.
1.2.1. Make sure the left gauge is around 20 psi. The metal valve opens when rotated clockwise.
1.2.2. Make sure that you close the nitrogen tank when you are done.
1.3. Open the VENT VALVE.
1.4. Wait until the chamber pressure reads 7.6 +2 (760 torr, this is atmospheric pressure)
1.5. Raise the bell jar a little bit using the RAISE button, and then turn off the VENT VALVE.
1.6. Raise the jar the rest of the way.

2. Prepare your sample

2.1. Look for a location on the plate where your sample will be shielded from the Gold AND Chrome when the SHUTTER is closed and exposed to the Gold AND Chrome when SHUTTER is open.
2.2. Tape your sample to that location using the VACUUM TAPE
2.3. Obtain both the GOLD BOAT and CHROME ROD located in the top drawer of a black shelf box.
2.4. Place the boats in their respective holders. Chrome in the back holder under the nut. Gold in the front holder under the wing nuts.
2.5. Make sure there is chrome on the tungsten rod, if it has been previously used it will have a green tint. If new it will be distinct coloration from the tungsten ends.
2.6. Add 2-3 gold beads to the gold boat each time.
2.7. If needed, replace the GLASS SLIDE WINDOW.

3. Check the CRYSTAL MONITOR (XTAL)

3.1. Turn on the INFICON monitor if it is not already on.
3.2. Push the XTAL button (button number 1), if the XTAL reading is 100%, change the CRYSTAL.

4. Pump down the CHAMBER

4.1. Lower the bell jar slowing using the LOWER button, make sure that the coating of the jar does not get caught on the sample holder. Make sure it makes a good seal.
4.2. Make sure the VENT VALVE is CLOSED.
4.3. SLOWLY open the ROUGHING PUMP VALVE and start a timer for T_{ROUGH} in the JIM logbook.
4.3.1. Keep the fore line pressure BELOW 3.0 +2.
4.4. When the pressure reads 5 -2 (50 mtorr) CLOSE the ROUGHING PUMP VALVE and record T_{ROUGH}.
4.5. Open the GATE VALVE and start T_{CRYO}.
4.6. Wait for ~30 seconds and turn on the ION GAUGE by pressing the EMIS button.
4.6.1. The filament should turn on, looking like a light bulb.
4.7. Wait until the chamber reaches 2.0 -6 ($2*10^{-6}$ torr), this usually takes around 120 minutes or so.

5. Deposition of Iron

5.1. Make sure that the INFICON monitor is on.
5.2. Iron should be program 2
5.3. Change the settings of DENISTY, Z-RATIO, and TOOLING FACTOR.
5.3.1. Press the PROG button.
5.3.2. Use the button that has a C with a triangle around it to go up in the menu, and the E with a triangle around it to go down until you are over the desired parameter.

5.3.3. To change the parameter, just type in the numbers. When the numbers are what they should be, hit the E triangle button.

Table 1*. Table of relevant values to input into the crystal monitor control panel for Iron*

Material	Density	Z-Ratio	Tooling
Iron	7.200	0.305	63.0

5.4. Flip the BOAT SELECTION toggle switch to the FRONT BOAT.
5.5. Flip the FILAMENT toggle switch to on. This turns on the power supply.
5.6. Ramp up the voltage with a maximum rate of 20 V/Min (5 V/15 Sec) using the VARIAC.
5.6.1. You should not exceed 10 Amps.
5.6.2. Go until you have a deposition rate of around 1-5Å/s. This can be seen on the INFICON monitor.
5.6.3. The voltage will usually be around 200-230 V.
5.7. OPEN the SHUTTER, and ZERO the crystal monitor (hit the 3 button that has the word ZERO over it).
5.8. Record everything in the logbook.
5.9. Wait until the INFICON monitor reads the desired thickness, usually around 0.020 kÅ (this is going to be 2 nm), then CLOSE the SHUTTER.
5.10. Ramp down the voltage at a rate LESS than 20 V/min.
5.11. Turn off the FILAMENT toggle switch.

6. Vent the chamber and remove sample
6.1. Get the chamber ready to be vented.
6.1.1. Turn OFF the ION GAUGE by hitting the EMIS button.
6.1.2. CLOSE the GATE VALVE toggle switch!
6.2. Open the Nitrogen Tank.
6.3. Open the VENT VALVE.
6.4. Wait until the chamber pressure reads 7.6 +2 (760 torr, this is atmospheric pressure)
6.5. Raise the bell jar a little bit using the RAISE button, and then turn off the VENT VALVE.
6.6. Raise the jar the rest of the way.

7. Get the system into standby
7.1. Lower the bell jar slowing using the LOWER button, make sure that the coating of the jar does not get caught on the sample holder. Make sure it makes a good seal.
7.2. Make sure the VENT VALVE is CLOSED.
7.3. SLOWLY open the ROUGHING PUMP VALVE
7.3.1. Keep the fore line pressure BELOW 3.0 +2.
7.4. When the pressure reads 5.0 -1 (0.5 torr) CLOSE the ROUGHING PUMP VALVE.
7.5. The system is now on standby.

8. **REMEMBER TO MAKE SURE THE NITROGEN TANK IS TRUNED OFF!! This includes the main valve on the far right, and the little black valve on the far left.**

S.O.P for CNT growth on transparent substrates

SOP for Furnace #1

Furnace Molten Golden Rules:

1. Never touch anything hot. I.e., a quartz boat, the quartz tube, or the inside of the furnace. Things may be hot even if they aren't glowing. Use tweezers to move the boat.
2. Never mix air with flammable gases (hydrogen or ethylene). Use argon to flush out the furnace in-between air and flammable gas. Leaks will inevitably mix air and flammable gas, and clogs will over pressurize the system until a fireball is released.

Furnace 1 is in U188, the one closest to the fume hood.

1. **Verify** that the furnace is on stand-by. Check the following: Furnace is off; temperature is below 200 C (red numbers); the tube is sealed; Argon, C_2H_4, and H_2 MFCs are off and the valves are closed (but do not overtighten the valves); air is flowing through the furnace; and the room ventilation is working properly.

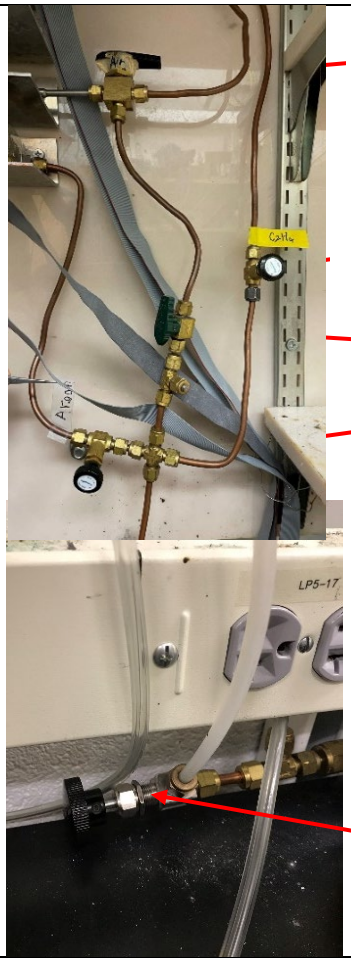

Figure 24) Valves for Furnace 1

2. **Verify** that the back endcap is sufficiently clean and not clogged by making sure that bubbles are **bubbling** in the Furnace 1 bubbler (second flask).
3. To **clean** the endcap, refer to the SOP for cleaning the end-cap. If you are not trained to do this, **contact** a furnace manager.

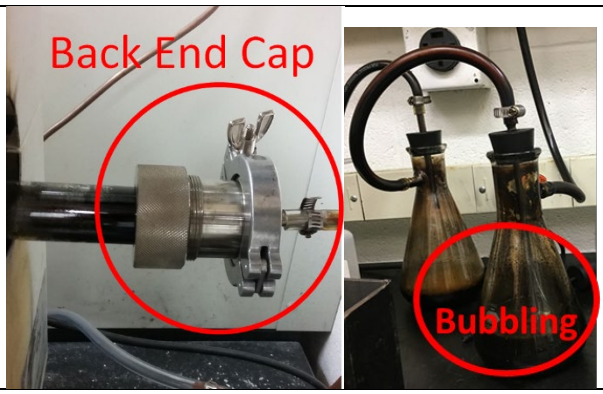

4. **Put on gloves.** Gloves keep you from touching hydrocarbons.
5. **Open the front-endcap** of the furnace by loosening the wingnut on the clamp. Push on the blank with your thumb to prevent it from falling when you remove the clamp. Then carefully remove the clamp and then the blank. Careful handling the blank so that the O-ring doesn't fall off of it. Do not unscrew the flange.

***Figure 25**) Endcaps for Furnace 1*

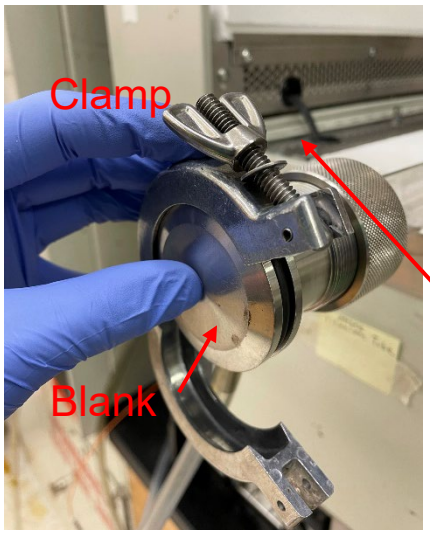

Hold the blank with your thumb so it doesn't fall when you take off the clamp.

Notice that the blank and the O-ring spacer are separate pieces. Be careful not to drop them.

6. **Open** the furnace lid. Always do so by grabbing the black handle on the front of the lid, and never inside the furnace.
7. **Pull** the quartz boat to the edge of the quartz tube using the hooked rod hanging on the wall. DO NOT TOUCH THE BOAT; IT MAY BE HOT! **Use tweezers** to remove the boat from the furnace and place it on the metal surface right next to the furnace.
8. **Place** your sample on the boat and put the boat inside the tube **using tweezers. Slide** the boat inside with the hooked rod. Center the tube inside the furnace so it sticks out equally in the front and back. Center the boat next to the thermocouple using the hooked rod. The boat should be level. Your sample should be centered on the boat and not touching the tube.
9. **Close** the front end-cap. As you tighten the wing nut, squeeze the clamp tightly so that the wing nut doesn't have to do all the work. Do not overtighten the wing nut because it can strip; it should just be snug and finger tight.
10. **Watch** if you can see the second flask start bubbling again. If not, make sure the front endcap is sealed and that the back endcap is not clogged. If the back endcap is clogged, see step 3.
11. **Open** gas cylinders: Argon, Ethylene (C_2H_4) and Hydrogen (H_2) in U187. First, verify that the regulator knob is loose (turn counterclockwise). Next, slowly open the main cylinder valve (turn counterclockwise) and then slowly increase the regulator pressure to 20 psi (turn clockwise).
    a. Do not open valves all the way. If a valve is stuck, don't force it. It might already be open. **Ask** the furnace manager for help.
    b. If the main cylinder pressure reads less than 200 psi, **ask** one of the furnace managers to replace the cylinder.

Figure 26)*Top) Endcap and O-ring for furnace 1. Bottom) Gas Cylinders for the furnaces*

Flush out the furnace with Argon:

12. **Open** the Argon valve (turn counterclockwise). Do not open needle valves all the way. (Note, the Argon MFC switch is broken so you can't turn it on and off with the switch. Just open and close the valve.)
13. **Turn off the air** MFC and **close the air** needle valve (different than the 3-way valve). Do not overtighten any of the valves. Let Argon flow for 10 seconds after the air is shut off before moving on.
    a. There should always be gas flowing to prevent backflow. For that reason, we start flowing Argon before we stop the air.

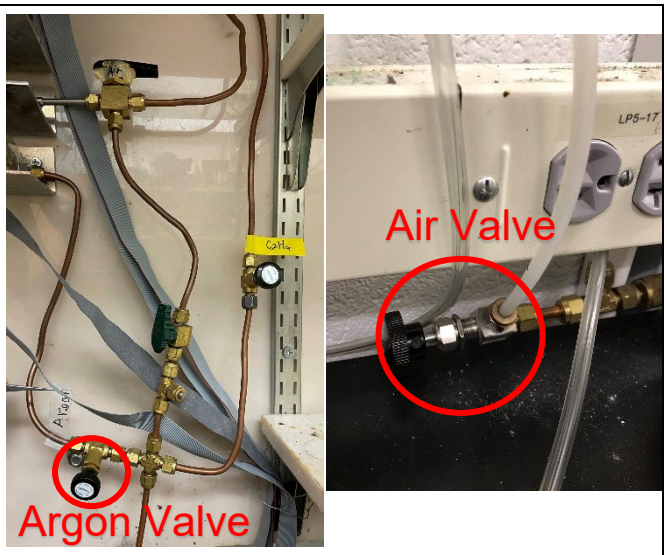

Figure 27) *Valves for furnace 1*

14. **Make sure** that the bubbler remains bubbling for the **duration** of the run. If there are no bubbles:
    a. The gas cylinder may be closed.
    b. The valve may be closed.
    c. The MFC switch may be off.
    d. There may be a very large leak (checking for bubbles does not catch small leaks).
    e. The back endcap may be clogged.

If a leak or clog happens during your run, immediately **leave** the room, **close** the gas cylinders in U187, and **contact** a furnace manager. Flammable gas leaks can catch fire and a clog can cause the endcap to pop off, releasing a fireball.

15. Argon should be the only gas flowing now. Valves should remain closed when not in use. **Turn** the three-way valve to "**H_2**" (pointing right).

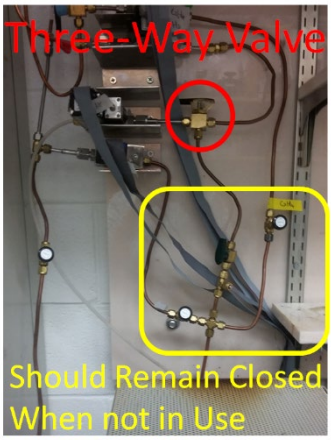

MFC (Mass Flow Controller) Setup:

16. Determine your desired gas flow. (**H_2 standard: 311 sccm**; **C_2H_4 standard: 338 sccm**.) To convert from sccm to MFC%, check the chart taped to the cabinet below the furnace, or visit https://nano.byu.edu/resources; Under "User Logs", click "Nanotube Growth" to open up the Furnace Log; go to the MFC Calibration tab and refer to the top (most recent) calibration table.
17. **Check** that all the MFCs are set to your desired flow rate. Flip the switch to "set" to see the set point. Then gently turn the knob to adjust the number on the screen. The black slider above the dial can lock the dial in place. Flip the switch back to "flow" when done. This displays the actual flow.

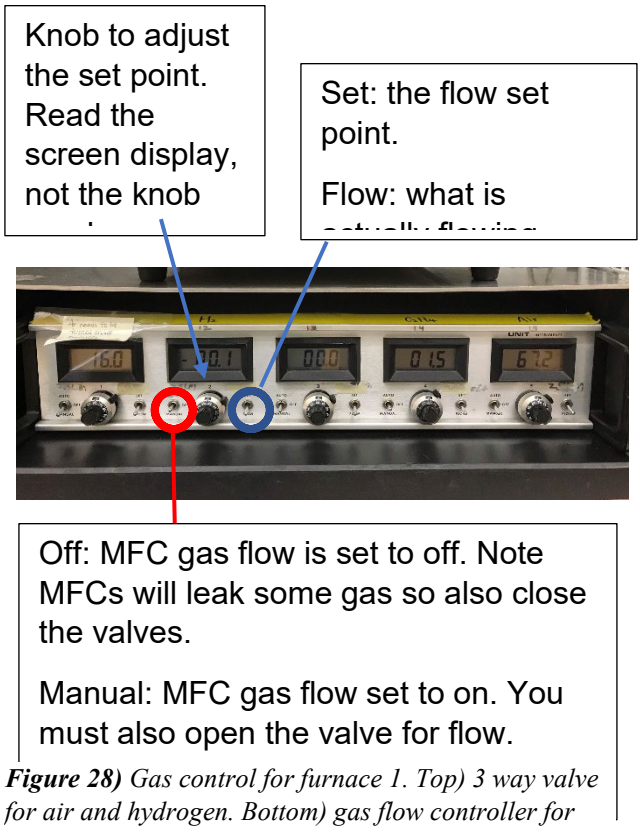

Figure 28) *Gas control for furnace 1. Top) 3 way valve for air and hydrogen. Bottom) gas flow controller for furnace 1.*

18. **Switch on H_2** by setting the switch to Manual (Manual=on).
19. **Open the C_2H_4** valve and **switch on the C_2H_4** MFC.

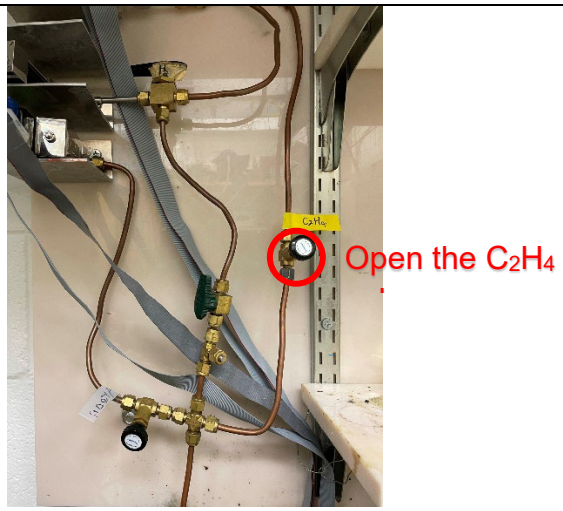

Figure 29) *C_2H_4 valve for furnace 1.*

20. **Go check** that the gas cylinder regulator pressures for H_2, C_2H_4, and Argon are still at 20 psi.
21. **Close the Argon** valve. H_2 and C_2H_4 should be the only gases flowing now.

22. Do a flammable gas **leak check** above the 2 endcaps and above the 2 flasks using the handheld flammable gas detector. Refer to the SOP for the flammable gas detector.
23. **Switch off the C_2H_4** MFC and **close the C_2H_4** valve. Now, H_2 should be the only gas flowing. THIS STEP IS EASY TO FORGET.

Figure 30) *Flammable gas leak checker*

24. **Set** the desired temperature. 750 C. This is done by holding the up or down arrows until the desired temperature is selected. A blinking decimal point indicates that the new temperature is unsaved. Press SET/ENT to save it. Do not heat the furnace above 900 C.
25. **Close** the furnace lid to start heating up the furnace. You should hear a clicking sound and the red light next to the switch will turn on. The OUT indicator light will turn on when the heating element is heating.
    a. Sometimes the furnace lid gets stuck on the tube. If this happens, gently shift the tube to the left or right so that the lid can close all the way. Careful not to rock the boat while adjusting the tube.

Display
Red: Actual Temp (C.)
Green: Set Point (C.)

Figure 31) *Furnace 1 controller*

26. **Don't stand or sit** in front of the furnace longer than you need to, in case the endcap pops off and a fireball comes out.
27. Once the temperature reaches the set point, **open the C_2H_4** valve and **switch on C_2H_4** to start the growth. **Start** your timer.

28. Once the growth is done, **switch off C_2H_4** and **close the C_2H_4** valve.
29. If you don't want to do a carbon infiltration, **skip** to step 34.
30. **Increase** the temperature to your desired infiltration temperature (Standard: 900 C). Don't go above 900 C. Keep H_2 on.
31. **Open the C_2H_4** valve and **switch on C_2H_4** (Standard: 338 sccm) to start the infiltration. **Start** your timer.
32. When desired infiltration is reached, **switch off C_2H_4** and **close the C_2H_4** valve.
33. **Set** the temperature to below 750 C (i.e., 700 C).
34. **Open the Argon** valve. **Switch off H_2**.
35. Once the temperature is at or below 750 C, **open** the furnace lid. Use the fan to speed up the cooling of the furnace. Place the fan on the metal blocks and set it to speed 2. Speed 3 will tip over the fan.
36. Once the temperature is below 200 C, **stop** the fan. You can put it on the floor to get it out of the way.
37. **Turn** the 3-way valve to **air**. **Open the air** valve. **Switch on the air**. **Switch off Argon** and **close the Argon** valve. Now, only air should be flowing.
38. **Open the front end-cap and unload** the sample. **Pull** the quartz boat to the front of the tube with the hooked rod. It is safer for your sample to slide the hooked rod below the boat instead of above it, but this method requires using one of the wider boats. DO NOT TOUCH THE BOAT; IT WILL BE HOT! **Use tweezers** to remove the boat from the furnace.
39. **Put** the quartz boat back in the middle of the furnace and **close the front end-cap**.
40. **Check** for bubbling. Air and only air should be flowing.
41. **Set** the temperature for the **cleaning process** (900 C after infiltration; 750 C after only growth) and **close** the furnace lid. While it is heating up, do steps 42 and 43.
42. **Fill out** the log. Go to "https://nano.byu.edu/resources"; Under "User Logs", click "Nanotube Growth". Fill out the spreadsheet.
43. **Ask** the other lab users if they are flowing gases. If no one else is using the gases, **close the gas cylinders**: **Release** the regulator pressure by turning the knob counterclockwise and then **close** the main cylinder valve by turning it clockwise. Do not overtighten valves.
44. **Slide** the tube until there is 1-2 inches between the metal casing of the furnace and the back end-cap. **Wait** until the back end of the tube is clean. It should be able to burn at least as far as the edge of the heating element coils. Then **slide** the tube until there is 1-2 inches between the metal casing of the furnace and the front end-cap. **Wait** until the front end of the tube is clean. Once the tube cleaning is complete, **slide** it to the central position.
45. **Open** the furnace lid and **cool down** to 200 C.
46. **Turn off** the furnace and then **close** the lid.
47. **Make sure** air is still flowing by checking that the bubbler is bubbling. Air should always be flowing when the furnace is not in use.

CAD models for Spectrometer holders

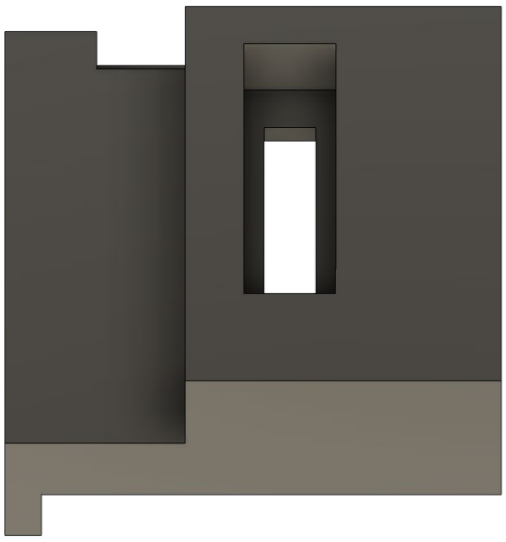

Figure 32). *CAD model of spectrometer holder for LEDs. A holder for the spectrometer with a flat to be able to place an LED board on.*

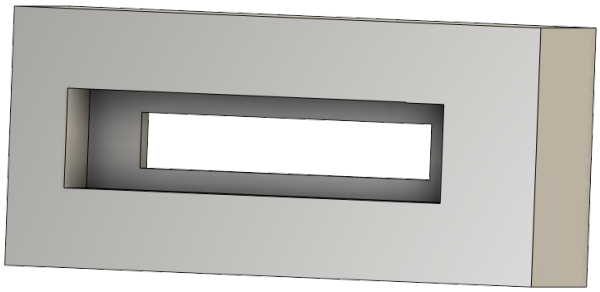

Figure 33). *CAD model of spectrometer holder. A spectrometer holder for experiments that do not require LEDs*

Matlab Script for Collimator Transmission

```
% define collimator
w=100; % opening in um
s=4; % wall in um
h=250; % height in um
%h=880; % Height for tall collimator in um
L=1000; % beam width, assume slitted in um
%L=10000; % beam width for IR
lam =  .650; % wavelength of input light in um (Use for v
%lam = 1.550; % IR

N=10000; %number of steps in angle.. this is the viewing screen number of pixels
Ntheta=30;
thetamax= Ntheta*lam/w; % range of angles to view, assume small angles, N times first zero of single slit
theta=linspace(-thetamax,thetamax,N+1);
%theta=linspace(-30/180*pi,30/180*pi,N+1);
xm=125000*theta;  %convert theta steps to physical size at screen. Visible
%xm=90000*theta;  %convert theta steps to physical size at screen.IR
det=4400; %size each way of detector in units of xm (Use with Vis data)
%det = 11200; % Size of Integrating sphere port (Use with IR data)

%Data collected for collimators
%Col1 is 100um x 880um illuminated by 650nm light
col1=[0.001667064
0.005477495
0.016908788
0.035960943
0.047392236
0.043581805
0.035960943
0.02452965
0.161705168
0.36937366
0.611336032
0.851393189
0.859014051
0.801857585
0.455108359
0.226482496
0.035960943
0.020719219
0.035960943
0.047392236
0.047392236
0.028340081
0.016908788
0.005477495];


ang1=[-22.5
-20.5
-18.5
-16.5
```

```
-14.5
-12.5
-10.5
-8.5
-6.5
-4.5
-2.5
-0.5
-0.5
1.5
3.5
5.5
7.5
9.5
11.5
13.5
15.5
17.5
19.5
21.5
];
%Collimator 2 100um x 880um in IR
ang2 = [-21.5
-19.5
-17.5
-15.5
-13.5
-11.5
-9.5
-7.5
-5.5
-3.5
-1.5
0.5
2.5
4.5
6.5
8.5
10.5
12.5
14.5
16.5
18.5];

col2 = [0
0.003621002
0
0.003621002
0.01931201
0
0
0.058539529
0.254677127
0.529269765
0.803862402
0.921544961
```

```
0.607724804
0.333132167
0.097767049
0.003621002
0.035003018
0.01931201
0.003621002
0
0];

%Collimator 3 is 100um pore 250 um tall measured in the IR

ang3 =[-21
-19
-17
-15
-13
-11
-9
-7
-5
-3
-1
1
3
5
7
9
11
13
15
17
19];

col3 = [0
0
0.071661238
0.218241042
0.315960912
0.413680782
0.511400651
0.609120521
0.706840391
0.804560261
0.951140065
0.90228013
0.804560261
0.706840391
0.609120521
0.511400651
0.413680782
0.315960912
0.218241042
0.120521173
0.052117264];
```

```
%Collimator 4 is 100 x 250um collimator illuminated with 650nm light
ang4=[-25.5
-23.5
-21.5
-19.5
-17.5
-15.5
-13.5
-11.5
-9.5
-7.5
-5.5
-3.5
-1.5
0.5
2.5
4.5
6.5
8.5
10.5
12.5
14.5
16.5
18.5
20.5
22.5
24.5];

col4= [-0.001396116
0.002411474
0
0.044294961
0.139484706
0.223251682
0.299403478
0.375555274
0.459322249
0.569742353
0.657316918
0.744891484
0.840081229
0.870541947
0.828658459
0.699200406
0.607818251
0.520243686
0.44409189
0.352709735
0.280365529
0.185175784
0.097601218
0.017641833
0
0];
```

```
err1 = .75*ones(size(ang1));
err2= .75*ones(size(ang2));
err3 = .75*ones(size(ang3));
err4 = .75*ones(size(ang4));

% single slit
alpha=sin(theta)*pi*w/lam;  %angle for sin(x)/x calculation
 slit=sin(alpha)./alpha; % finish sin(x)/x
% slit=sin(alpha-.2)./(alpha-.2);
slit=min(1,slit); %force peak value to 1, make it defined
slit2=slit.^2;  %convert to intensity
%figure
%plot(xm,slit2/sum(slit2))
%hold on
%title([num2str(w) ' w ' num2str(s) ' s ' num2str(h) ' h ' num2str(L) ' L '])
%xlabel('units of mm')
% axis([-10 10 0 12])
%axis([min(xm) max(xm) 0 12])

% beam
alphab=sin(theta)*pi*L/lam;  %angle for beam spread
beam=sin(alphab)./alphab; % intensity distribution for beam spread
%plot(theta,beam,'r-')

% array
C=thetamax/asin(lam/(s+w)); %number of array peaks in angular range
C=round(C);
%arrayspace=asin(lam/(s+w));

%tilt range setup
tltmax=asin(w/h); %max is the cutoff angle
Ntilt=200;  %~number of tilt angle calculations

%tlfig=figure('Position',[605 671 560 420]);

%splfig=figure('Position',[15 671 560 420]);

for j=0:Ntilt
 tltangle=j/Ntilt*tltmax;
 tlt(j+1)=tltangle/pi*180;  %convert tiltangle to degrees
 wnew=w-h*sin(tltangle);  %new width of slit.
 speriod=(s+w)*cos(tltangle); % new periodicity of array
 pp(j+1)=speriod; %periodity array for that tilt
 wp(j+1)=wnew; %width array for that tilt
 arrayspace=asin(lam/speriod);  %spacing of array peaks

 alpha=sin(theta)*pi*wnew/lam; %angle for single slit
 slitnew=sin(alpha)./alpha; %intensity for single slit with new width
 slitnew=min(1,slitnew); %fix zero location
 slitnew2=slitnew.^2;

%plot(xm,wnew*slitnew2/sum(slitnew2)) %plot single slit
 Int=zeros(size(theta)); %initialize array to zeros
```

```
for i=-C:C  % sum over possible peaks in array

   shift=(arrayspace*i)*pi*L/lam; %angle for this peak
%    Int=Int+min(1,sin(alphab-shift)./(alphab-shift)); %add beam intensities at location of array point
   Int=Int+min(1,exp(-((alphab-shift).^2)/10)); %add beam intensities at location of array point
end
%Intt=(Int).^2;
Intt=(Int.*slitnew).^2;  %impose single slit envelope and square
if j==0
   othax=Int.*slitnew;
end
Int2=Intt./sum(Intt)*wnew/(s+w);  %normalize and then shrink according to open area

twod=((Int.*slitnew)'*othax).^2;
twod=twod*wnew^2/(s+w)^2;
%figure(splfig)
%imagesc(twod(1500:3500,1500:3500)',[0 .002])

int3(j+1)=sum(Int2.*(xm>-det & xm<det));
%figure(tlfig)
%plot(xm,Int2,'g-')
%hold on
%plot(xm,(othax.^2)./sum(othax.^2)*w/(s+w),'r-')
%axis([min(xm) max(xm) 0 0.01])
%axis([min(xm)/4 max(xm)/4 0 0.01])
%  axis([-50 50 0 .2])
%title([num2str(tltangle/pi*180) ' tilt(degrees) ' num2str(wnew) ' wnew ' num2str(speriod) ' speriod '])
%plot([-det -det det det],[0.2 0 0 0.2],'k-')
%pause(.001)
%hold off
end

%figure
%plot(pp,'r-')
%hold on
%plot(wp,'g-')
%hold off

figure
plot(tlt,int3,'r-')
hold on
%plot([tltmax/pi*180 tltmax/pi*180], [0 max(int3)],'r-')
plot([0 tltmax/pi*180],[((w/(s+w))^2) 0],'k-')

errorbar(ang4,col4,err4,'Horizontal','b.','MarkerSize',10)
plot(-tlt,int3,'r-')
plot([0 -tltmax/pi*180],[(w/(s+w))^2 0],'k-')
plot([0 -tltmax*1/pi*180],[(w/(s+w))^2 0],'k-')
plot([0 tltmax*1/pi*180],[((w/(s+w))^2) 0],'k-')

tltmax2=asin(w/275); %275 um tall collimator
```

```
h=285; % height in um

theta=linspace(-thetamax,thetamax,N+1);
% single slit
alpha=sin(theta)*pi*w/lam;  %angle for sin(x)/x calculation
 slit=sin(alpha)./alpha; % finish sin(x)/x
% slit=sin(alpha-.2)./(alpha-.2);
slit=min(1,slit); %force peak value to 1, make it defined
slit2=slit.^2;  %convert to intentsity


% beam
alphab=sin(theta)*pi*L/lam;  %angle for beam spread
beam=sin(alphab)./alphab; % intensity distribution for beam spread
%plot(theta,beam,'r-')

% array
C=thetamax/asin(lam/(s+w)); %number of array peaks in angular range
C=round(C);
%arrayspace=asin(lam/(s+w));

%tilt range setup
tltmax=asin(w/h); %max is the cutoff angle
Ntilt=30;  %~number of tilt angle calculations



for j=0:Ntilt
 tltangle2=j/Ntilt*tltmax;
 tltf(j+1)=tltangle2/pi*180;  %convert tiltangle to degrees
 wnew=w-h*sin(tltangle2);  %new width of slit.
 speriod=(s+w)*cos(tltangle2); % new periodicity of array
 ppf(j+1)=speriod; %periodity array for that tilt
 wpf(j+1)=wnew; %width array for that tilt
 arrayspace=asin(lam/speriod);  %spacing of array peaks

 alpha=sin(theta)*pi*wnew/lam; %angle for single slit
 slitnew=sin(alpha)./alpha; %intensity for single slit with new width
 slitnew=min(1,slitnew); %fix zero location
 slitnew2=slitnew.^2;

%plot(xm,wnew*slitnew2/sum(slitnew2)) %plot single slit
 Int=zeros(size(theta)); %initialize array to zeros
for i=-C:C  % sum over possible peaks in array

    shift=(arrayspace*i)*pi*L/lam; %angle for this peak
%    Int=Int+min(1,sin(alphab-shift)./(alphab-shift)); %add beam intensities at location of array point
    Int=Int+min(1,exp(-((alphab-shift).^2)/10)); %add beam intensities at location of array point
end
%Intt=(Int).^2;
Intt=(Int.*slitnew).^2;  %impose single slit envelope and square
if j==0
    othax=Int.*slitnew;
end
```

```
Int2=Intt./sum(Intt)*wnew/(s+w);  %normalize and then shrink according to open area

twod=((Int.*slitnew)'*othax).^2;
twod=twod*wnew^2/(s+w)^2;
%figure(splfig)
%imagesc(twod(1500:3500,1500:3500)',[0 .002])

int3f(j+1)=sum(Int2.*(xm>-det & xm<det));
%figure(tlfig)
%plot(xm,Int2,'g-')
%hold on
%plot(xm,(othax.^2)./sum(othax.^2)*w/(s+w),'r-')
%axis([min(xm) max(xm) 0 0.01])
%axis([min(xm)/4 max(xm)/4 0 0.01])
%  axis([-50 50 0 .2])
%title([num2str(tltangle/pi*180) ' tilt(degrees) ' num2str(wnew) ' wnew ' num2str(speriod) ' speriod '])
%plot([-det -det det det],[0.2 0 0 0.2],'k-')
%pause(.001)
%hold off
end
plot(tltf,int3f,'.','Color',[0.4660 0.6740 0.1880])
plot(-tltf,int3f,'.','Color',[0.4660 0.6740 0.1880])

title('100um x 250um Collimator with 650nm Illumination')
xlabel('Angle (Degrees)')
ylabel('Relative Intensity (%)')
% legend({'Geometric Model with Diffraction Correction', 'Geometric Model', 'Measured Transmission
Data','Diffraction Correction Model 275um Tall Collimator'},'Location', 'NorthWest')
hold off

hold off
```

Python Script for LVF model

```
import math
import functools

import numpy as np
from scipy.optimize import minimize_scalar
from matplotlib import pyplot as plt

def d_csmax(t, w, h, n_cs, n_plastic):
    theta_pmax = math.atan(w/h)
    return t / (math.tan(math.asin(n_plastic * math.sin(theta_pmax) / n_cs)))

# lambda_effective - the value for lambda as if it were normal incidence.
# this is calculated for the purpose of using the result as an input to
# I_filter, which assumes normal incidence
# n_filter means index of refraction in the optical filter
def lambda_eff(lambda_air, theta_air, n_filter):
    theta_f = math.asin(math.sin(theta_air) / n_filter)
    return lambda_air * (1-(1/n_filter)**2 * math.sin(theta_air)**2)**(1/2)

# lambda_0 meaning the wavelength about which the filter is centered.
# In the context of a variable filter, this is where on on the filter
# is the measurement being taken.
#
# lambda_in is the effective wavelength subjected to the filter, if
# the angle of incidence is not normal, then this is lambda_eff above
#
# this function is a placeholder, using an approximate function
# that attempts to match what is shown in the data sheet for the filter
```

```
# in consideration.
# for REO VariFi, see https://www.reoinc.com/files/REO_VarFi_Data_Sheet.pdf
#   - 1-2% FWHM
#   - ~90% transmission at peak, although this varies over the spectrum

def I_filter(lambda_0, lambda_in):
  #  return 0.5 * math.exp(-(abs(lambda_in - lambda_0)) / (2 * (0.003 * lambda_0)**2)) + \
  # return 0.9 * math.exp(-(abs(lambda_in - lambda_0)**2) / (2 * (0.01 * lambda_0)**2))
   #return 0.6 * math.exp(-(abs(lambda_in - lambda_0)) / (2 * (0.003 * lambda_in)**2)) + \
       #   0.3 * math.exp(-(abs(lambda_in - lambda_0)**3) / (2 * (0.02 * lambda_in)**2))
   return 1/(1+1013*math.sin((4*3.14*lambda_0/lambda_in)/2)**2)

# instensity due to shadowing effect of collimator (assumes rectangular grid)
def I_theta_n(theta_n, n_plastic, h, w):
   return max(0, 1 - h / w * math.tan(math.asin(math.sin(theta_n) / n_plastic)))

# instensity due to combined shadowing effect of collimator in x and y directions (assumes rectangular grid)
# units of h and w are irrelevant, they divide out
# n_plastic is the index of refraction of the material that fills the collimator pores
def I_theta(theta_air_x, theta_air_y, n_plastic, h, w):
   return I_theta_n(theta_air_x, n_plastic, h, w) * I_theta_n(theta_air_y, n_plastic, h, w)

# assumes rectangular grid, t is width of walls, w is dimensions of pores
def I_open(t, w):
   return w**2 / (t + w)**2

# this is just accounting for power loss (1/r^2)
def I_spherical(theta_air, n_plastic, h):
   theta_plastic = math.asin(math.sin(theta_air) / n_plastic)
```

```
    return (math.cos(theta_plastic) / h)**2


# assume random/unpolarized light
# equations source: http://hyperphysics.phy-astr.gsu.edu/hbase/phyopt/freseq.html
# also https://www.rp-photonics.com/fresnel_equations.html
# question ... they hyperphysics version fails when theta = 0, but the other doesn't. Am I overlooking something?
def I_trans(theta_1, n_1, n_2):
    theta_2 = math.asin(n_1 / n_2 * math.sin(theta_1))
    t_s = 2 * n_1 * math.cos(theta_1) / (n_1 * math.cos(theta_1) + n_2 * math.cos(theta_2))
    T_s = t_s**2 * n_2 * math.cos(theta_2) / (n_1 * math.cos(theta_1))
    t_p = 2 * n_1 * math.cos(theta_1) / (n_1 * math.cos(theta_2) + n_2 * math.cos(theta_1))
    T_p = t_p**2 * n_2 * math.cos(theta_2) / (n_1 * math.cos(theta_1))
    return (T_s + T_p) / 2



# one interface (at filter)
def I_trans_no_col(theta_air, n_filter):
    return I_trans(theta_air, 1, n_filter)


# two interfaces (at plastic and at filter)
def I_trans_w_col(theta_air, n_plastic, n_filter):
    air_plastic = I_trans(theta_air, 1, n_plastic)
    theta_plastic = math.asin(1 / n_plastic * math.sin(theta_air))
    # plastic_filter = I_trans(theta_plastic, n_plastic, n_filter)
    return air_plastic #* plastic_filter


# I_spherical is not included since assuming negligable distance between source and filter, and therefore negligable difference with angle
def I_no_col(lambda_0, lambda_air, theta_air, n_filter):
    return I_filter(lambda_0, lambda_eff(lambda_air, theta_air, n_filter)) * \
```

```
        I_trans_no_col(theta_air, n_filter) # effect was not significant..


def I_w_col(lambda_0, lambda_air, theta_air, theta_air_x, theta_air_y, n_filter, n_plastic, h, w, t):
    return I_filter(lambda_0, lambda_eff(lambda_air, theta_air, n_filter)) * \
            I_theta(theta_air_x, theta_air_y, n_plastic, h, w) * \
            I_open(t, w) * \
            I_trans_w_col(theta_air, n_plastic, n_filter)
            # leaving out for now
            # doesn't seem to change shape.. makes harder to compare with no_col,
            # I_spherical(theta_air, n_plastic, h)



# run simulation from 60 to 0 degrees (calc at 0 is counted half and the whole is mult * 2 to account for 0 to 60 degrees)
# run simulation from .7 to 1.2 times lambda_0
# Simulation is only run in 1 dimension (imagine imaging sensor as a line in space)
# ignoring reflectivity for now
# let total intensity over line segment of width 'w' be 1.
def simulate_no_col(res, lambda_0):
    result = {} # a set of bins and intensity for lambda_air values computed
    n_filter = 1.33 # just a guess for now
    for lambda_air in np.arange(math.floor(0.92 * lambda_0), math.ceil(1.08 * lambda_0), res):
        result[lambda_air] = 0
        for theta_air in np.arange(0, 50, res):
            intensity = I_no_col(lambda_0, lambda_air, math.radians(theta_air), n_filter)
            if theta_air == 0:
                result[lambda_air] += intensity
            result[lambda_air] += 2 * intensity
    return list(zip(*result.items()))
```

```
def simulate_h_col13(adc13, res, lambda_0, h=None, w=None, t=None, n_plastic=None, n_filter=None):
    result = {} # a set of bins and intensity for lambda_air values computed

    for lambda_air in np.arange(math.floor(0.92 * lambda_0), math.ceil(1.08 * lambda_0), res):
        result[lambda_air] = 200
        for theta_air in np.arange(0, 50, res):
            intensity = I_w_col(lambda_0,
                                lambda_air,
                                math.radians(theta_air),
                                math.radians(theta_air),
                                0, n_filter,
                                n_plastic,
                                h,
                                w,
                                t)
            if theta_air == 0:
                result[lambda_air] += intensity
            result[lambda_air] += 2 * intensity*adc13
    return list(zip(*result.items()))

# for 1000 nm
def simulate_h_col10(adc10, res, lambda_0, h=None, w=None, t=None, n_plastic=None, n_filter=None):
    result = {} # a set of bins and intensity for lambda_air values computed

    for lambda_air in np.arange(math.floor(0.92 * lambda_0), math.ceil(1.08 * lambda_0), res):
        result[lambda_air] = 400
        for theta_air in np.arange(0, 50, res):
            intensity = I_w_col(lambda_0,
                                lambda_air,
                                math.radians(theta_air),
```

```
                    math.radians(theta_air),
                    0, n_filter,
                    n_plastic,
                    h,
                    w,
                    t)
        if theta_air == 0:
            result[lambda_air] += intensity
        result[lambda_air] += 2 * intensity*adc10
    return list(zip(*result.items()))
#for 1100nm
def simulate_h_col11(adc11, res, lambda_0, h=None, w=None, t=None, n_plastic=None, n_filter=None):
    result = {} # a set of bins and intensity for lambda_air values computed

    for lambda_air in np.arange(math.floor(0.92 * lambda_0), math.ceil(1.08 * lambda_0), res):
        result[lambda_air] = 300
        for theta_air in np.arange(0, 50, res):
            intensity = I_w_col(lambda_0,
                    lambda_air,
                    math.radians(theta_air),
                    math.radians(theta_air),
                    0, n_filter,
                    n_plastic,
                    h,
                    w,
                    t)
        if theta_air == 0:
            result[lambda_air] += intensity
        result[lambda_air] += 2 * intensity*adc11
    return list(zip(*result.items()))
```

```
# For 1200 nm
def simulate_h_col12(adc12, res, lambda_0, h=None, w=None, t=None, n_plastic=None, n_filter=None):
    result = {} # a set of bins and intensity for lambda_air values computed

    for lambda_air in np.arange(math.floor(0.92 * lambda_0), math.ceil(1.08 * lambda_0), res):
        result[lambda_air] = 200
        for theta_air in np.arange(0, 50, res):
            intensity = I_w_col(lambda_0,
                                lambda_air,
                                math.radians(theta_air),
                                math.radians(theta_air),
                                0, n_filter,
                                n_plastic,
                                h,
                                w,
                                t)
            if theta_air == 0:
                result[lambda_air] += intensity
            result[lambda_air] += 2 * intensity*adc12
    return list(zip(*result.items()))

#For 1400 nm
def simulate_h_col14(adc14, res, lambda_0, h=None, w=None, t=None, n_plastic=None, n_filter=None):
    result = {} # a set of bins and intensity for lambda_air values computed

    for lambda_air in np.arange(math.floor(0.92 * lambda_0), math.ceil(1.08 * lambda_0), res):
        result[lambda_air] = 0
        for theta_air in np.arange(0, 50, res):
            intensity = I_w_col(lambda_0,
                                lambda_air,
```

```
                    math.radians(theta_air),
                    math.radians(theta_air),
                    0, n_filter,
                    n_plastic,
                    h,
                    w,
                    t)
        if theta_air == 0:
            result[lambda_air] += intensity
        result[lambda_air] += 2 * intensity*adc14
    return list(zip(*result.items()))

#For 1500 nm
def simulate_h_col15(adc15, res, lambda_0, h=None, w=None, t=None, n_plastic=None, n_filter=None):
    result = {} # a set of bins and intensity for lambda_air values computed

    for lambda_air in np.arange(math.floor(0.92 * lambda_0), math.ceil(1.08 * lambda_0), res):
        result[lambda_air] = 200
        for theta_air in np.arange(0, 50, res):
            intensity = I_w_col(lambda_0,
                    lambda_air,
                    math.radians(theta_air),
                    math.radians(theta_air),
                    0, n_filter,
                    n_plastic,
                    h,
                    w,
                    t)
            if theta_air == 0:
                result[lambda_air] += intensity
```

```
            result[lambda_air] += 2 * intensity*adc15
    return list(zip(*result.items()))


# plot original filter width vs with varying theta (no collimator and with collimator)
res = .5
h = 250
w = 100
t = 5
n_filter = 1.33
n_plastic = 1
lambda_0 = 1300
# plt.plot(*simulate_ref(lambda_0), 'g-')
#plt.title("{} nm bandpass filter, \ncollimator h={}, w={}, t={}, n_plastic={},
n_filter={}".format(lambda_0, "variable", w, t, n_plastic, n_filter))
#plt.plot(*simulate_no_col(res, lambda_0), 'b',  dashes=[1, 2, 10, 2], label="no collimator")


# for n in np.arange(1, 2, .1):
#     plt.plot(*simulate_w_col(res, lambda_0, h=h, w=w, t=t, n_plastic=n, n_filter=n_filter), label="n_p =
{:.2f}".format(n))


# # for patent varying n_plastic
# n = 1
# plt.plot(*simulate_w_col(res, lambda_0, h=h, w=w, t=t, n_plastic=n, n_filter=n_filter), 'r',  dashes=[3,
2, 10, 2], label="n_p = {:.2f}".format(n))
# n = 2
# plt.plot(*simulate_w_col(res, lambda_0, h=h, w=w, t=t, n_plastic=n, n_filter=n_filter), 'g',  dashes=[2,
2], label="n_p = {:.2f}".format(n))


# for w in np.arange(20, 200, 20):
#     plt.plot(*simulate_w_col(res, lambda_0, h=h, w=w, t=t, n_plastic=n_plastic, n_filter=n_filter),
label="w = {}".format(w))
```

lambda1 =
[900,904.8,909.6,914.4,920.2,926,931.8,937.6,943.4,949.2,955,960.8,966.6,972.4,978.2,984,989.8,995.6,
1001.4,1007.2,1013,1018.8,1024.6,1030.4,1036.2,1042,1047.8,1053.6,1059.4,1065.2,1071,1076.8,1082.6
,1088.4,1094.2,1100,1105.8,1111.6,1117.4,1124.2,1131,1138.8,1144.6,1151.4,1160.2,1167,1172.8,1179.
6,1185.4,1191.2,1197,1202.8,1208.6,1214.4,1220.2,1226,1231.8,1237.6,1243.4,1250.2,1256,1266.8,1272
.6,1278.4,1285.2,1292,1297.8,1303.6,1309.4,1315.2,1321,1326.8,1332.6,1338.4,1344.2,1349,1354.8,136
1.6,1372.4,1378.2,1384,1389.8,1395.6,1401.4,1407.2,1413,1418.8,1424.6,1430.4,1436.2,1442,1447.8,14
53.6,1465.4,1471.2,1477,1482.8,1488.6,1494.4,1500.2,1506,1511.8,1517.6,1523.4,1529.2,1535,1540.8,1
546.6,1552.4,1558.2,1564,1569.8,1575.6,1581.4,1587.2,1593,1598.8,1604.6,1610.4,1616.2,1622,1627.8,
1633.6,1639.4,1645.2,1651,1656.8,1662.6];

col13=(675,660,748,577,601,620,635,626,722,572,641,703,638,550,472,399,510,443,497,538,438,410,4
71,474,433,426,464,373,400,455,427,375,336,364,386,407,310,392,335,353,304,322,275,229,355,177,27
0,339,356,302,280,339,346,364,265,255,195,270,298,306,194,304,255,193,359,736,1943,2238,1466,937,
612,468,416,411,400,321,314,376,328,271,288,143,227,240,240,224,276,220,328,146,258,297,254,220,3
32,175,279,276,215,199,334,114,248,261,227,325,271,153,241,204,233,309,159,308,140,273,265,284,27
3,288,220,354,334,299,285,378,308,250);

col10=[679,734,768,651,623,680,802,656,786,557,676,636,622,481,541,444,611,722,1026,1010,742,652
,635,526,480,427,526,437,479,472,497,420,378,490,367,455,394,404,446,462,379,444,296,272,433,270,
282,385,408,363,312,395,324,374,352,371,254,366,459,396,242,334,267,138,435,318,224,232,420,412,3
22,347,358,351,327,382,308,386,350,270,348,239,291,348,366,345,369,244,456,172,296,319,303,212,38
1,237,386,348,344,270,388,145,294,244,370,479,329,337,310,231,282,378,250,369,245,364,397,393,375
,298,279,401,375,353,404,374,398,343]

col11=[726,772,778,732,687,733,782,689,746,615,703,634,718,471,499,435,570,539,551,580,463,484,5
07,556,432,478,408,446,486,510,540,491,398,812,1510,1619,1171,784,668,523,432,383,380,326,449,25
2,335,395,452,399,363,422,407,334,362,363,291,408,431,389,218,356,315,190,355,266,212,228,400,423
,346,392,310,371,313,333,286,437,355,209,342,217,271,338,389,352,387,257,488,227,354,365,300,214,
379,219,370,332,337,278,372,205,315,249,246,431,308,305,328,281,312,380,196,371,242,390,377,397,3
30,257,284,446,372,433,379,400,436,269]

col12=[736,724,788,743,655,727,757,658,748,638,682,690,696,509,558,504,540,510,550,577,511,484,5
67,497,476,463,425,410,462,541,474,449,427,468,392,437,426,418,359,411,380,385,342,325,412,252,32
2,424,504,798,1854,2066,1382,903,611,465,420,514,424,362,296,390,300,173,377,288,293,274,386,428,
284,349,358,332,340,304,251,335,395,310,293,269,295,277,331,316,257,244,402,193,343,333,277,154,3
67,256,330,310,364,317,364,165,325,251,297,377,395,269,296,291,278,338,231,317,228,268,370,383,35
7,243,251,375,412,367,323,380,371,333]

col14=[481,460,467,428,372,476,368,308,366,437,262,461,376,323,317,242,256,237,262,395,341,279,2
92,286,291,226,228,242,100,176,208,172,128,196,132,157,59,168,43,168,-
9,70,93,137,83,125,82,69,143,25,35,39,66,29,35,-37,90,63,62,-40,53,36,6,65,15,21,-39,21,18,15,51,-
21,58,-21,-
13,135,46,53,26,74,126,360,1532,2252,1455,725,398,279,268,128,129,145,26,0,30,102,34,22,16,-
31,32,50,46,108,8,87,104,30,-12,-4,140,10,85,59,106,46,8,12,50,65,-24,65,-18,-67,-3,40,3,69]

col15=[712,706,764,597,597,728,680,609,700,569,621,629,622,612,486,399,490,468,514,546,419,406,4
49,524,344,448,416,418,348,386,384,304,298,374,364,333,260,288,290,278,228,271,279,209,279,253,23

```
1,231,278,281,178,270,227,210,169,179,193,210,254,198,175,258,142,29,269,156,180,167,176,248,250,
212,185,168,184,233,204,268,307,232,216,172,184,222,156,231,209,165,348,142,170,217,206,144,111,1
61,289,622,1684,2276,1677,922,571,467,306,382,344,266,264,223,249,177,164,230,226,237,222,230,27
8,267,159,319,250,329,239,276,231,201]


# Optimize adc

def objective12(adc12):

    points = np.column_stack((lambda1, col12))

    curve = np.array(simulate_h_col12(adc12, res, 1200, h=h, w=w, t=t, n_plastic=n_plastic,
n_filter=n_filter)).T


    # Filter the points to be the ones that we care about (the peaks)

    points = points[points[:,1] > 1000, :]


    # print(points.shape)

    # print(curve.shape)


    # Make the "difference" tensor

    A = points[:, None, :] - curve[None, :, :]


    # print(A.shape)


    # Take the norm of each vector

    A = np.linalg.norm(A, axis=2)


    # print(A.shape)


    # Take the minimal norm from each point

    norms = np.min(A, axis=1)


    # print(norms.shape)
```

```
    # Sum the norms
    return np.sum(norms)


adc12 = minimize_scalar(objective12).x
print(adc12)


def objective14(adc14):
    points = np.column_stack((lambda1, col14))
    curve = np.array(simulate_h_col14(adc14, res, 1400, h=h, w=w, t=t, n_plastic=n_plastic,
n_filter=n_filter)).T


    # Filter the points to be the ones that we care about (the peaks)
    points = points[points[:,1] > 700, :]


    # print(points.shape)
    # print(curve.shape)


    # Make the "difference" tensor
    A = points[:, None, :] - curve[None, :, :]


    # print(A.shape)


    # Take the norm of each vector
    A = np.linalg.norm(A, axis=2)


    # print(A.shape)


    # Take the minimal norm from each point
    norms = np.min(A, axis=1)
```

```
    # print(norms.shape)

    # Sum the norms
    return np.sum(norms)

adc14 = minimize_scalar(objective14).x
print(adc14)

# Optimize adc
def objective13(adc13):
    points = np.column_stack((lambda1, col13))
    curve = np.array(simulate_h_col13(adc13, res, 1300, h=h, w=w, t=t, n_plastic=n_plastic,
n_filter=n_filter)).T

    # Filter the points to be the ones that we care about (the peaks)
    points = points[points[:,1] > 500, :]

    # print(points.shape)
    # print(curve.shape)

    # Make the "difference" tensor
    A = points[:, None, :] - curve[None, :, :]

    # print(A.shape)

    # Take the norm of each vector
    A = np.linalg.norm(A, axis=2)

    # print(A.shape)
```

```
    # Take the minimal norm from each point
    norms = np.min(A, axis=1)

    # print(norms.shape)

    # Sum the norms
    return np.sum(norms)

adc13 = minimize_scalar(objective13).x
print(adc13)

def objective10(adc10):
    points = np.column_stack((lambda1, col10))
    curve = np.array(simulate_h_col10(adc10, res, 1000, h=h, w=w, t=t, n_plastic=n_plastic,
n_filter=n_filter)).T

    # Filter the points to be the ones that we care about (the peaks)
    points = points[points[:,1] > 700, :]

    # print(points.shape)
    # print(curve.shape)

    # Make the "difference" tensor
    A = points[:, None, :] - curve[None, :, :]

    # print(A.shape)

    # Take the norm of each vector
    A = np.linalg.norm(A, axis=2)
```

```
    # print(A.shape)

    # Take the minimal norm from each point
    norms = np.min(A, axis=1)

    print(norms.shape)

    # Sum the norms
    return np.sum(norms)

adc10 = minimize_scalar(objective10).x
print(adc10)

def objective11(adc11):
    points = np.column_stack((lambda1, col11))
    curve = np.array(simulate_h_col11(adc11, res, 1100, h=h, w=w, t=t, n_plastic=n_plastic,
n_filter=n_filter)).T

    # Filter the points to be the ones that we care about (the peaks)
    points = points[points[:,1] > 1100, :]

    # print(points.shape)
    # print(curve.shape)

    # Make the "difference" tensor
    A11 = points[:, None, :] - curve[None, :, :]

    # print(A.shape)
```

```
    # Take the norm of each vector
    A11 = np.linalg.norm(A11, axis=2)

    # print(A.shape)

    # Take the minimal norm from each point
    norms11 = np.min(A11, axis=1)

    # print(norms.shape)

    # Sum the norms
    return np.sum(norms11)

adc11 = minimize_scalar(objective11).x
print(adc11)

def objective15(adc15):
    points = np.column_stack((lambda1, col15))
    curve = np.array(simulate_h_col15(adc15, res, 1500, h=h, w=w, t=t, n_plastic=n_plastic,
n_filter=n_filter)).T

    # Filter the points to be the ones that we care about (the peaks)
    points = points[points[:,1] > 500, :]

    # print(points.shape)
    # print(curve.shape)

    # Make the "difference" tensor
    A = points[:, None, :] - curve[None, :, :]
```

```
    # print(A.shape)

    # Take the norm of each vector
    A = np.linalg.norm(A, axis=2)

    # print(A.shape)

    # Take the minimal norm from each point
    norms = np.min(A, axis=1)

    # print(norms.shape)

    # Sum the norms
    return np.sum(norms)

adc15 = minimize_scalar(objective15).x
print(adc15)



# # for patent varying w
h = 400
plt.plot(*simulate_h_col13(adc13, res, 1300, h=h, w=w, t=t, n_plastic=n_plastic, n_filter=n_filter), 'b')
plt.plot(*simulate_h_col10(30, res, 1000, h=h, w=w, t=t, n_plastic=n_plastic, n_filter=n_filter), 'orange')
plt.plot(*simulate_h_col11(60, res, 1100, h=h, w=w, t=t, n_plastic=n_plastic, n_filter=n_filter), 'g')
plt.plot(*simulate_h_col12(adc12, res, 1200, h=h, w=w, t=t, n_plastic=n_plastic, n_filter=n_filter), 'red')
plt.plot(*simulate_h_col14(adc14, res, 1400, h=h, w=w, t=t, n_plastic=n_plastic, n_filter=n_filter),
'purple')
plt.plot(*simulate_h_col15(adc15, res, 1500, h=h, w=w, t=t, n_plastic=n_plastic, n_filter=n_filter),
'brown')
plt.scatter(lambda1,col13,marker = 'o',s=30)
```

```
plt.scatter(lambda1,col10,marker = 'o')
plt.scatter(lambda1,col11,marker = 'o')
plt.scatter(lambda1,col12,marker = 'o')
plt.scatter(lambda1,col14,marker = 'o')
plt.scatter(lambda1,col15,marker = 'o')
#plt.legend()
plt.ylabel(" intensity (A/D counts)")
plt.xlabel("wavelength (nm)")
plt.show()
```

Schematic for Teensy board

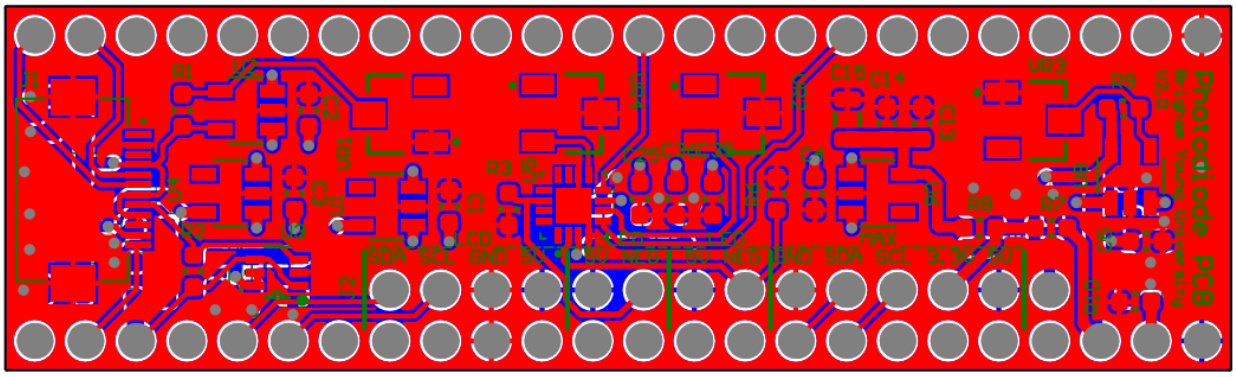

Figure 34) *Board layout for Teensy interface board used for data collection with miniaturized spectrometer*

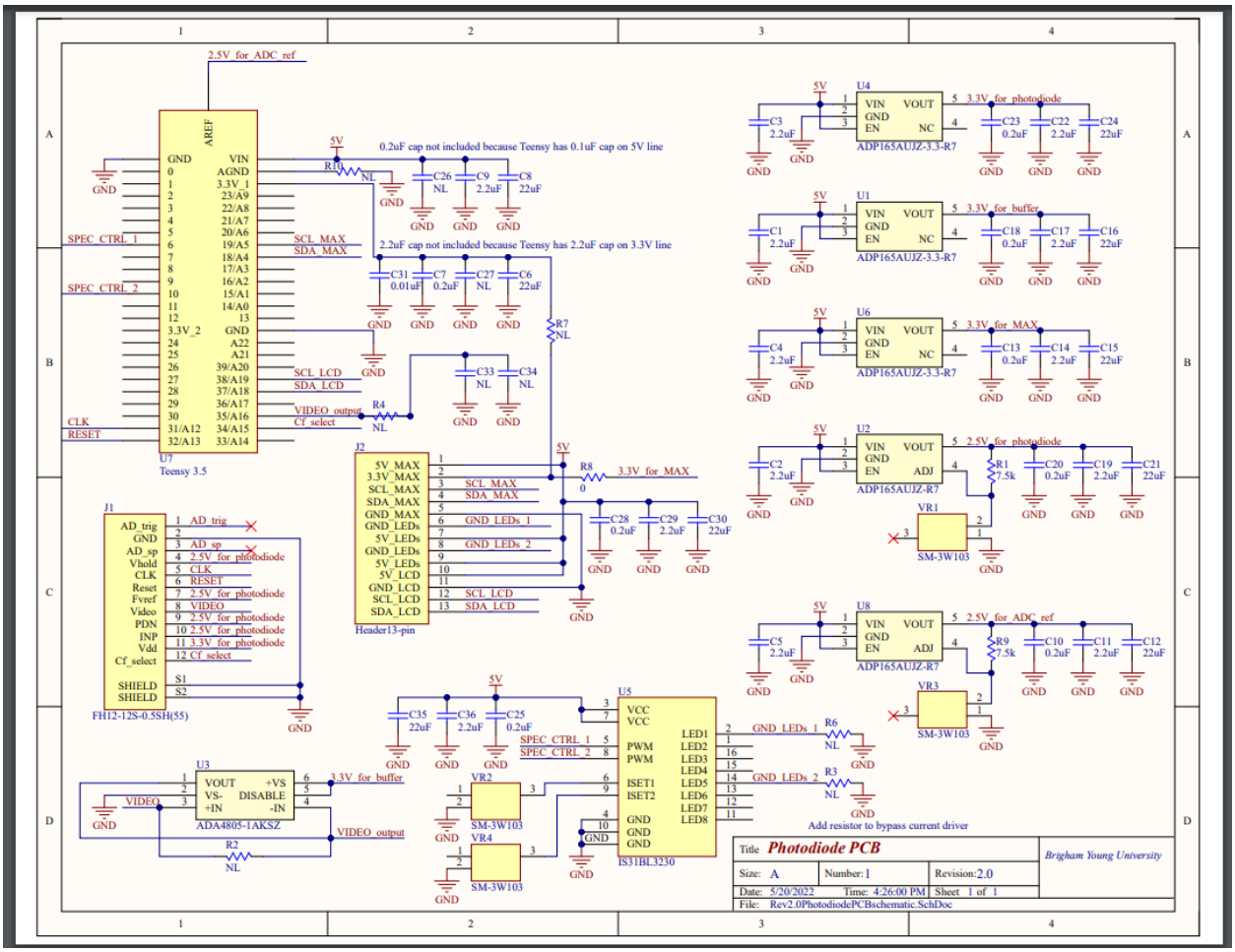

Figure 35) *Layout for Teensy interface board used for data collection with miniaturized spectrometer*